

Lattice QCD at finite temperature and density

Owe Philipsen^a

Institut für Theoretische Physik, Universität Münster, D-48149 Münster, Germany

Abstract. QCD at finite temperature and density is becoming increasingly important for various experimental programmes, ranging from heavy ion physics to astro-particle physics. The non-perturbative nature of non-abelian quantum field theories at finite temperature leaves lattice QCD as the only tool by which we may hope to come to reliable predictions from first principles. This requires careful extrapolations to the thermodynamic, chiral and continuum limits in order to eliminate systematic effects introduced by the discretization procedure. After an introduction to lattice QCD at finite temperature and density, its possibilities and current systematic limitations, a review of present numerical results is given. In particular, plasma properties such as the equation of state, screening masses, static quark free energies and spectral functions are discussed, as well as the critical temperature and the QCD phase structure at zero and finite density.

1 Introduction

Quantum chromodynamics (QCD) is the theory of the strong interactions, describing nuclear matter in terms of its constituent quarks and gluons and their interactions. One of its key features is asymptotic freedom, *i.e.* the fact that the coupling strength is decreasing as a function of momentum transfer of an interaction. Thus, while the theory is amenable to perturbation theory at large momenta, it is non-perturbative for energy scales $\lesssim 1$ GeV and lattice QCD is the only known method for first principles calculations in this regime.

At a critical temperature $T_c \approx 200$ MeV, QCD predicts a transition between the familiar confined hadron physics and a deconfined phase of quark gluon plasma (QGP). At the same temperature, the weakly broken chiral symmetry, responsible for the three light pions, gets restored. QCD at high temperatures is of outstanding importance in today's theoretical and experimental nuclear and particle physics programmes. A thermal environment with sufficiently high temperatures for a QCD plasma has certainly existed during the early stages of the universe, which passed through the quark hadron transition on its way to its present state. Current and future heavy ion collision experiments are recreating this primordial plasma at RHIC (BNL), LHC (CERN) and FAIR (GSI). These studies will have a bearing far beyond QCD in the context of early universe and astro-particle physics. Many prominent features of the observable universe, such as the baryon asymmetry or the seeding for structure formation, have been determined primordially in hot plasmas described by non-abelian gauge theories. The QCD plasma serves as a prototype for those, since it is the only one we can hope to produce in laboratory experiments. Moreover, certain QCD plasma properties entering calculations of dark matter abundances need to be known at percent level accuracy in order to match the ever more precise astro-physical data expected in the near future [1]. On the other hand, for high densities and low temperatures, exotic non-hadronic phases such as a color superconductor have been predicted [2], and such physics might be realized in the cores of compact stars.

^a e-mail: o.philipsen@uni-muenster.de

For these applications we need to know how the properties of QCD change under extreme conditions of temperature and density. This entails a determination of the QCD phase diagram and the associated critical properties, a quantitative understanding of the equation of state, the way in which hadron properties get modified as well as the nature of the lightest excitations in non-hadronic phases.

Early hopes that the high temperature plasma phase might be accessible to perturbation theory have proved wrong, as we shall see. Indeed, today one rather speaks of the strongly coupled quark gluon plasma (sQGP). This leaves lattice QCD as the main computational tool even in that regime. However, lattice simulations are still struggling with limitations and systematic errors. For example, only in the last few years has it become possible to perform simulations for QCD at small baryon density, while the case of cold and high density matter remains inaccessible to date. These lectures are intended to provide an introduction to the problems tackled by lattice simulations, their potential and limitations, as well as an overview over current results.

2 Finite temperature QCD in the continuum and on the lattice

2.1 QCD at finite temperature and density

The thermodynamics of QCD is most conveniently described by the grand canonical partition function [3]

$$Z(V, \mu_f, T; g, m_f,) = \text{Tr} \left(e^{-(H - \mu_f Q_f)/T} \right) = \int DA D\bar{\psi} D\psi e^{-S_g[A_\mu]} e^{-S_f[\bar{\psi}, \psi, A_\mu]}, \quad (1)$$

with the euclidean gauge and fermion actions

$$S_g[A_\mu] = \int_0^{1/T} dx_0 \int_V d^3x \frac{1}{2} \text{Tr} F_{\mu\nu} F_{\mu\nu},$$

$$S_f[\bar{\psi}, \psi, A_\mu] = \int_0^{1/T} dx_0 \int_V d^3x \sum_{f=1}^{N_f} \bar{\psi}_f (\gamma_\mu D_\mu + m_f - \mu_f \gamma_0) \psi_f. \quad (2)$$

The partition function depends on the external macroscopic parameters T, V, μ_f , as well as on the microscopic parameters like masses and the coupling constant. The index f labels the different quark flavours, and the conserved quark numbers corresponding to the chemical potentials μ_f are $Q_f = \psi \gamma_0 \psi$. In the following we will consider mostly two and three flavours of quarks, and always take $m_u = m_d$. The case $m_s = m_{u,d}$ is then denoted by $N_f = 3$, while $N_f = 2 + 1$ implies $m_s \neq m_{u,d}$. For our purposes we will couple all flavours to the same chemical potential μ unless otherwise stated. The chemical potential for baryon number is then $\mu_B = 3\mu$. Once the partition function is known, thermodynamic properties such as free energy, pressure, average particle numbers or the thermal expectation value of an operator O readily follow,

$$F = -T \ln Z, \quad P = \frac{\partial(T \ln Z)}{\partial V}, \quad \langle Q_f \rangle = \frac{\partial(T \ln Z)}{\partial \mu_f}, \quad \langle O \rangle = Z^{-1} \text{Tr}(O e^{-(H - \mu_f Q_f)/T}). \quad (3)$$

In the thermodynamic limit $V \rightarrow \infty$, we are interested in the corresponding densities, *i.e.* $f = F/V, p = P/V = -f, \dots$

While the formulation of QCD thermodynamics is straightforward, controlled evaluations are prohibitively difficult. Perturbation theory, the tool so successful for electroweak physics at zero temperature, fails us completely in this context. The reasons are two-fold. Firstly, the running coupling is still not weak enough at temperature scales of interest, $g(100-300\text{MeV}) \sim 1$. Worse still is the fact that finite T perturbation theory for non-abelian gauge theories displays

an insurmountable infrared problem [4]. At finite T , a gauge boson self coupling gets dressed with a thermal distribution function which for small momenta behaves as

$$\frac{g^2}{e^{E/T} - 1} \underset{E, p \ll T}{\sim} \frac{g^2 T}{m}. \quad (4)$$

Thus, the effective expansion parameter diverges for perturbatively zero mass particles such as gluons, no matter how weak the coupling, *i.e.* this problem also exists in the symmetric electroweak phase. Higher orders do generate an effective gluonic mass scale $m \sim g^2 T$ to cure this divergence, and resummation methods have been devised to calculate it [5]. But now the coupling cancels out of the expansion parameter and all loop orders contribute in the same way, leaving convergence of such series unclear. Hence, a fully non-perturbative treatment of the problem is warranted.

2.2 The Lattice Formulation

The thermal quantum field theory is discretized by introducing a euclidean space-time lattice $L^3 \times N_t$ with lattice spacing a , such that volume and temperature are

$$V = (aL)^3, \quad T = \frac{1}{aN_t}. \quad (5)$$

The fermion fields live on the lattice sites x , whereas the gauge fields are represented by link variables $U_\mu(x) \in SU(3)$ connecting the sites. The simplest actions used in many thermodynamics calculations are the Wilson gauge action and the staggered, or Kogut-Susskind, fermion action

$$S_g[U] = \sum_x \sum_{1 \leq \mu < \nu \leq 4} \beta \left(1 - \frac{1}{3} \text{Re Tr } U_p \right), \quad S_f^{KS} = \sum_{x,y} \bar{\chi}(x) M_{xy} \chi(y), \quad (6)$$

respectively. Here $U_p = U_\mu(x) U_\nu(x + a\hat{\mu}) U_\mu^\dagger(x + a\hat{\nu}) U_\nu^\dagger(x)$ is the elementary plaquette and the bare lattice and continuum gauge couplings are related by $\beta = 6/g^2$. The staggered fermion matrix is given by

$$M_{xy}(m_f, \tilde{\mu}) = \frac{1}{2} \sum_{\mu=1}^3 (-1)^{x_0 + \dots + x_{\mu-1}} (\delta_{x+\hat{\mu}, y} U_\mu(x) - \delta_{x, y+\hat{\mu}} U_\mu(y)^\dagger) \\ + \frac{1}{2} (\delta_{x+\hat{0}, y} U_0(x) e^{a\mu} - \delta_{x, y+\hat{0}} U_0(y)^\dagger e^{-a\mu}) + \delta_{xy} a m_f. \quad (7)$$

Note that the chemical potential $a\mu$ enters through the temporal links only [6]. Now the Gaussian integral over the quark fields can be performed, leading to the partition function

$$Z(L, a\mu, N_t; \beta, N_f, a m_f) = \int DU \prod_f (\det M(m_f, \mu))^{1/4} e^{-S_g[U]}. \quad (8)$$

The lattice action is not unique, any action reproducing the continuum action in the limit $a \rightarrow 0$ is in principle admissible. We refer to textbooks [7] for discussions of various actions and their advantages/disadvantages, as well as the daunting task of a chiral fermion formulation. While the above staggered fermions have a remnant $U(1)$ chiral symmetry, they also exhibit spurious flavours (called tastes) which then have to be removed by taking the fourth root of the fermion determinant in Eq. (8). It is not yet settled whether this produces potentially hazardous non-localities or singularities, a subject of much current debate [8]. Things empirically seem to work well as long as continuum limits are taken before chiral limits. On the other hand, Wilson fermions do not require roots of determinants, but they break chiral symmetry completely at finite lattice spacing and require additive quark mass renormalization. They also feature so-called exceptional configurations with negative eigenvalues of the determinant,

making simulations with light quarks very difficult. There are also fermion actions avoiding those issues, such as domain wall fermions or overlap fermions, for reviews see [9,10]. However, at the present stage these actions are an order of magnitude more costly in simulation time and hence not yet widely used for dynamical thermodynamics simulations. It is for this reason that most results quoted in this review have been produced with staggered or Wilson fermions and their improved variants. The non-uniqueness of lattice actions can be exploited to construct actions which remove the $O(a)$, $O(a^2)$... corrections to continuum results, thus improving the approach to the continuum limit. Introductions to improvement can be found in [11].

2.3 Constraints on lattice simulations and systematic errors

It is important to realize from the outset that current lattice simulations, and especially those at finite temperature and density, are still hampered by systematic errors and uncertainties. Let us discuss the origins of those. The Compton wave length of a hadron is proportional to its inverse mass, $\sim m_H^{-1}$, and the largest of those constitutes the correlation length of the statistical system. To keep finite size as well as discretization errors under control, we need to require

$$a \ll m_H^{-1} \ll aL. \quad (9)$$

Typical lattice sizes today are $(12-32)^3 \times 4$, $16^3 \times 8$ etc., depending on computing budgets and machines. For temperatures around $T \sim 200$ MeV, Eq. (5) with $N_t = 4-6$ implies $a \sim 0.1-0.3$ fm and $aL \sim 1.5-3$ fm. For the low T phase, Eq. (9) then tells us that the lightest hadron needs to be $m_\pi \gtrsim 250$ MeV. The push to do physical quark masses is only just beginning to be a possibility on the most powerful machines and with the cheapest actions (*i.e.* staggered, with Wilson rapidly catching up). On the other hand, at high T screening masses scale as $m_H \sim T$ requiring $N_t^{-1} \ll 1 \ll LN_t^{-1}$. Hence, the spatial lattice size should be significantly larger than the temporal one. This limits the feasible temperatures to several T_c .

Once the simulations have been carried out, all quantities appear in lattice units, *i.e.* as dimensionless numbers, and need to be translated to physical units. This procedure of “setting the scale” introduces additional systematic errors, which are often much larger than the statistical errors of the simulations. Suppose we want to convert some measured critical temperature to physical units. It thus needs to be related to a quantity whose value in nature we know and which can also be obtained from a lattice simulation, for example a hadron mass at zero temperature,

$$\frac{T}{m_H} = \frac{1}{N_t(am_H)}. \quad (10)$$

In practice this is difficult, because QCD with physical parameters is not quite doable numerically yet. Moreover, one is often interested in the limit of heavy or zero quark masses, or with two or three degenerate flavours. In such cases one uses quantities related to the static potential, such as the string tension σ or the Sommer scale r_0 [12], which strictly speaking only exist in the pure gauge or heavy quark effective theories,

$$\frac{T}{\sqrt{\sigma}} = \frac{1}{(a\sqrt{\sigma})N_t}, \quad \sqrt{\sigma} \approx 425 \text{ MeV}; \quad Tr_0 = \frac{r_0}{aN_t} \quad \text{with} \quad r^2 \frac{dV(r)}{dr} \Big|_{r=r_0} = 1.65. \quad (11)$$

The values are provided through analyses of heavy quark effective theories applied to b -quark systems, *e.g.* [13]. Fortunately the string tension turns out to be rather insensitive to the presence of light quarks, *i.e.* it is approximately the same independent of the quark content of QCD.

Another difficulty arises for extrapolations to the continuum limit. Given some temperature T , the lattice spacing is set via $T = 1/(aN_t)$, which then controls the gauge coupling $\beta = 6/g^2(a)$. Thus, changing β changes temperature for a lattice with fixed N_t . As a consequence, the cut-off in a simulation at fixed N_t varies as a function of temperature. *E.g.*, if a simulation is performed for a set of quark masses fixed in lattice units, $am_f = \text{const}$, then changing

$a(T)$ implies that the quark mass in physical units changes as well! In principle this can be avoided by simulating along the “lines of constant physics”, *i.e.* tuning bare masses together with the lattice spacing such that the masses in physical units stay constant. In practice, this is a formidable task since the lines of constant physics are, of course, not known and have to be mapped out non-perturbatively first. Again, simulations along lines of constant physics are only just being started.

2.4 Finite baryon density and the sign problem

As soon as a chemical potential for quark number is switched on, $\mu \neq 0$, a Monte Carlo evaluation of the partition function eq. (8) is essentially impossible due to the so-called sign problem of QCD. The problem is encapsulated in the γ_5 -hermiticity of the Dirac operator,

$$\mathcal{D}(\mu)^\dagger = \gamma_5 \mathcal{D}(-\mu^*) \gamma_5, \quad (12)$$

which implies that $\det M$ is complex for the gauge group $SU(3)$ and $\mu \neq 0$. Note that the partition function and all physical observables remain real, *i.e.* the imaginary parts of the determinant cancel out once they are averaged over all gauge configurations. However, in a Monte Carlo evaluation using importance sampling, the determinant is evaluated in the background of single gauge configurations and interpreted as part of the probability weight for that configuration. This is impossible if the determinant is complex. Methods to circumvent this problem will be discussed in sec. 5.

2.5 The quenched limit, the chiral limit and physical QCD

Much of our intuition regarding the quark hadron transition is based on the limiting cases of infinite or zero quark masses, *i.e.* the quenched (or static quark) and chiral limits, respectively. In these cases there exist true order parameters and the phase structure and transition can be discussed qualitatively based on symmetry breaking and universality arguments.

For infinitely heavy quarks QCD reduces to Yang-Mills theory in the presence of static sources. The static quark propagator is given by a Wilson line closing through the time boundary, *i.e.* the Polyakov loop,

$$L(\mathbf{x}) = \prod_{x_0}^{N_t} U_0(x). \quad (13)$$

The action displays a global symmetry under center transformations $U_0(x) \rightarrow z_n U_0(x)$, with $z_n = \exp i2\pi n/3 \in Z(3)$. On the other hand, static sources transform non-trivially, $L(\mathbf{x}) \rightarrow z_n L(\mathbf{x})$. The free energy of a static quark is given by [14]

$$\langle \text{Tr } L(\mathbf{x}) \rangle \sim e^{-\frac{F_q}{T}}, \quad (14)$$

and constitutes an order parameter for confinement, *i.e.* $\langle L \rangle = 0$ for $T < T_c$, and $\langle L \rangle \neq 0$ for $T > T_c$. Hence there must be a true non-analytic phase transition corresponding to the breaking of the $Z(3)$ symmetry. One can construct an effective theory for the order parameter reflecting its $Z(3)$ symmetry [15], and universality arguments suggest a first order phase transition. This is indeed borne out by simulations.

In the limit of zero quark masses the classical QCD Lagrangian is invariant under global chiral symmetry transformations, the total symmetry being $U_A(1) \times SU_L(N_f) \times SU_R(N_f)$. The axial $U_A(1)$ is anomalous, quantum corrections break it down to $Z(N_f)$. The remainder gets spontaneously broken to the diagonal subgroup, $SU_L(N_f) \times SU_R(N_f) \rightarrow SU_V(N_f)$, giving rise to $N_f^2 - 1$ massless Goldstone bosons, the pions. The order parameter signalling chiral symmetry is the chiral condensate,

$$\langle \bar{\psi} \psi \rangle = \frac{1}{L^3 N_t} \frac{\partial}{\partial m_f} \ln Z. \quad (15)$$

It is nonzero for $T < T_c$, when chiral symmetry is spontaneously broken, and zero for $T > T_c$. Effective models for the order parameter in this case are thus $O(2N_f)$ linear sigma models [16]. The finite temperature phase transition then corresponds to chiral symmetry restoration.

QCD with physical quark masses obviously does not correspond to either limit. The $Z(3)$ symmetry is explicitly broken once there are dynamical fermions, and the chiral symmetry is broken by non-zero quark mass terms. Nevertheless, physical QCD displays confinement as well as three very light pions as “remnants” of those symmetries. In the presence of mass terms there is no true order parameter, *i.e.* the expectation values of the Polyakov loop as well as the chiral condensate are non-zero everywhere. Hence the deconfined or chirally symmetric phase is analytically connected with the confined or chirally broken phase, and there is no need for a non-analytic phase transition. The following questions then arise, which should be answered by numerical simulations: for which parameter values of QCD is there a true phase transition, and what is its order? Are confinement and chirality changing across the same single transition or are there different ones? If there is just one transition, which is the driving mechanism? If there is only a smooth crossover, how do the properties of matter change?

2.6 Effective high T theory: dimensional reduction

As we have seen, systematics presently constrain simulations of lattice QCD to temperatures below a few times T_c . However, for applications to early universe physics, as well as our own understanding and comparisons with perturbation theory, we would also like to have non-perturbative information at much higher temperatures. This can be achieved by means of effective field theories. At large T , when the gauge coupling $g(T)$ is sufficiently small, a hierarchy between different relevant scales of thermal QCD develops,

$$2\pi T \gg gT \gg g^2 T. \quad (16)$$

The lowest non-vanishing bosonic Matsubara mode $\sim 2\pi T$ is characteristic for non-interacting particles. The dynamics generates the Debye scale $m_E \sim gT$, over which color electric fields A_0 are screened, and its non-perturbative analogue $m_M \sim g^2 T$ for color magnetic fields A_i [4].

For physics on scales larger than the inverse temperature, $|\mathbf{x}| \sim 1/gT \gg 1/T$, this allows an effective theory approach in which the calculations are factorized: integration over the hard modes may be performed perturbatively by expanding in powers of the ratio of scales $gT/(2\pi T) \sim g/(2\pi)$. This includes all non-zero Matsubara modes, in particular the fermions. It results in a 3d effective theory for modes $\sim gT$ and softer,

$$S_{eff} = \int d^3x \left\{ \frac{1}{2} \text{Tr}(F_{ij}F_{ij}) + \text{Tr}(D_i A_0)^2 + m_E^2 \text{Tr}(A_0^2) + \lambda_3 (\text{Tr}(A_0^2))^2 \right\}, \quad (17)$$

and is known as dimensional reduction [17]. Since 4d euclidean time has been integrated over, A_0 now appears as an adjoint scalar, and the effective parameters are functions of the original ones, $g_3^2 = g^2 T$, $m_E(N, N_f, g, m_q^f) \sim gT$, $\lambda_3(N, N_f, g, m_q^f) \sim g^4 T$.

Discretization and simulation of this reduced problem is easy. Without fermions and in one dimension less, much larger volumes and finer lattices can be employed. Moreover, 3d gauge theories are superrenormalizable and the coupling scales linearly with lattice spacing. Hence, very accurate continuum limits can be obtained and systematic errors from simulations can be eliminated. However, the reduction step entails two approximations: the perturbative computation is limited to a finite order in g and neglects higher-dimensional operators, which are suppressed by powers of the scale ratio. The reduction step has been performed up to two-loop order [18] at which parameters have relative accuracy $\mathcal{O}(g^4)$, while for correlation functions the error is [19] $\delta C/C \sim \mathcal{O}(g^3)$. In the treatment of the electroweak phase transition, this is less than 5% [20], for QCD it depends on the size of the coupling $g(T)$ and thus on T . It has been non-perturbatively checked by comparing simulations in 4d with those of the 3d effective theory, that the latter accurately reproduces static correlation lengths at temperatures as low as $T \gtrsim 2T_c$ [21,22], thus allowing for a straightforward treatment of very large temperatures as well as detailed dynamical investigations in the plasma phase.

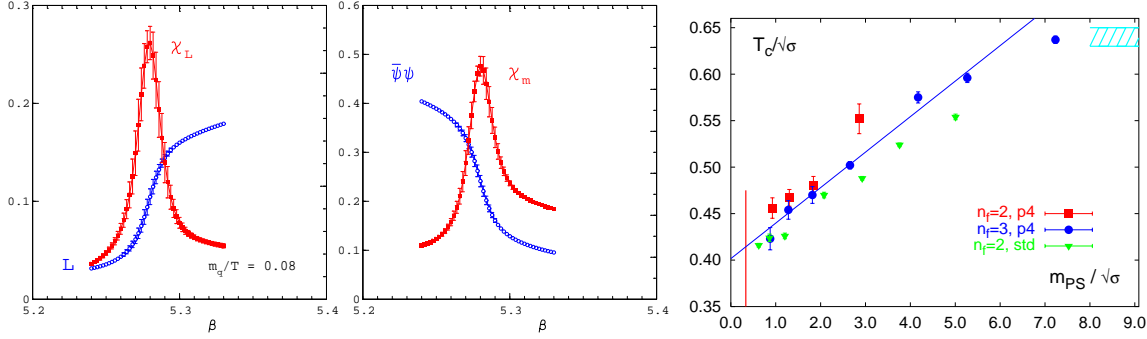


Fig. 1. The order parameters for deconfinement $\langle L \rangle$ (left) and chiral symmetry restoration $\langle \bar{\psi}\psi \rangle$ (middle), together with their susceptibilities as a function of the gauge coupling for two-flavour QCD. From [23]. Right: Quark mass dependence of T_c for $N_f = 2, 3$ with improved (p4) and standard staggered quarks. From [28].

3 Numerical results at finite T and $\mu = 0$

3.1 The (pseudo-) critical temperature

The first task when investigating finite temperature QCD is to find the phase boundary. Thus, for QCD with a fixed quark content, we are interested in the critical (or pseudo-critical) temperature where the transition from the confining regime to the plasma regime takes place. The method to locate a transition usually is to look for rapid changes of observables like the Polyakov loop L , the chiral condensate or the plaquette, and for peaks of their fluctuations, *i.e.* the generalized susceptibilities

$$\chi_O = VN_t \langle (O - \langle O \rangle)^2 \rangle. \quad (18)$$

The locations of these peaks define (pseudo-)critical couplings β_c which can be turned into temperatures through the knowledge of a zero temperature quantity like a hadron mass $am_H(\beta_c)$ at the same coupling, $T_c/m_H = 1/(N_t am_H(\beta_c))$. In practice, often the two-loop beta function is used as a short cut, although this becomes valid only when the lattice spacing is fine enough to be in the perturbative regime.

On coarse lattices $N_t = 4, 6$, all numerical evidence is consistent with confining and chiral properties changing at approximately the same β_c . An example is shown in fig. 1 (left and middle) for two-flavour QCD. On finite volumes, true non-analytic phase transitions do not exist and the identified phase boundary represents only a crossover. The nature and critical properties of the transition can be obtained from scaling behaviour of various quantities with volume and quark mass, as will be discussed in sec. 4.

T_c for the pure $SU(3)$ gauge theory has been known rather precisely for quite a while [24,25]. It has since then been confirmed by studies using various improved actions, thus reducing finite lattice spacing effects. The number is most readily given in terms of the string tension,

$$T_c/\sqrt{\sigma} = 0.632 \pm 0.002, \quad (19)$$

which was obtained as a weighted average over all available lattice data [26]. For QCD with dynamical quarks, one finds T_c to be increasing with quark mass, as shown in fig. 1 (right). The data correspond to one lattice spacing only, *i.e.* are not yet continuum results. Extrapolating the results to the chiral limit, one obtains

$$\begin{aligned} \underline{\text{2-flavor QCD}} : T_c &= \begin{cases} (171 \pm 4) \text{ MeV,} & \text{clover-improved Wilson [27]} \\ (173 \pm 8) \text{ MeV,} & \text{improved staggered [28]} \end{cases} \\ \underline{\text{3-flavor QCD}} : T_c &= (154 \pm 8) \text{ MeV, improved staggered [28]} \end{aligned}$$

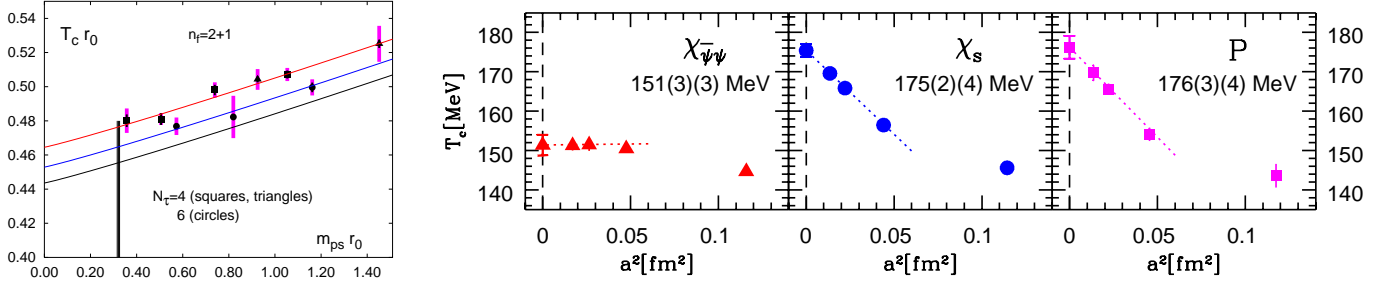


Fig. 2. Left: T_c in units of r_0 as a function of pseudo-scalar mass for lattices with $N_t = 4, 6$. The vertical line shows the physical value $m_{PS} r_0 = 0.321(5)$. From [29]. Right: Continuum extrapolations of T_c , determined from susceptibilities of the chiral condensate, the strange quark susceptibility and the Polyakov loop for physical quark masses. From [30].

where m_ρ has been used to set the scale. In view of the systematic errors introduced by the discretization of the fermion sector, it is reassuring that consistent results are obtained from staggered and Wilson fermions. Qualitatively we see that adding light degrees of freedom reduces the critical temperature for the transition.

Having studied the flavour and quark mass dependence of T_c , the phenomenologically important quantity is of course T_c for physical quark masses in the continuum limit. Two recent works have pushed in this direction [29,30], and the comparison of the two is an interesting illustration of systematic effects in lattice calculations. The authors of [29] have worked with two lattice spacings $N_t = 4, 6$, with the strange quark mass tuned to its physical value and a range of light quark masses, $am_{u,d} = 0.1 - 0.4 m_s$. Critical couplings are determined from peaks of chiral and Polyakov loop susceptibilities and found to be consistent with each other. They are then converted to temperature via a renormalization group improved two-loop beta function and the scale is set by r_0 (cf. sec. 2.3). Finally, a combined extrapolation to the continuum and chiral limits is performed, as shown in fig. 2 (left), leading to the prediction $T_c = 192(7)(4)$ MeV.

A different number is quoted in [30]. In this work four lattice spacings are considered, $N_t = 4, 6, 8, 10$, for which the quark masses are tuned along the lines of constant physics, such that the meson masses correspond to nearly their physical values on all lattices. The critical couplings are determined through the chiral and strange quark susceptibility, as well as from the steepest change of the Polyakov loop. This is done for all lattice spacings, followed by a continuum extrapolation, as shown in fig. 2 (right). The scale in this work is set by the kaon decay constant f_K , and the final value is based on the extrapolation of the chiral condensate, $T_c = 151(3)(3)$. There are two striking observations to be made. Firstly, the $N_t = 4$ data do not fall onto the straight a^2 -extrapolation line to the continuum limit, *i.e.* are not in the scaling region yet. Second, when finer lattices are considered, different observables lead to different critical temperatures. This is to be expected for a crossover, where T_c is only pseudo-critical and not uniquely defined. As we shall see in sec. 4, this is the situation for physical QCD. Nevertheless, the gap is larger than expected, and also the ordering is puzzling: it suggests that there is a temperature range still displaying confinement while chiral symmetry is already restored, which goes against conventional wisdom. As a potential source for the discrepancy with [29], the authors of [30] identify cut-off effects, as is illustrated in fig. 3. If the continuum extrapolation is performed with two different methods to set the scale, then the data of [29] appear to lead to inconsistent results. Likewise, a continuum extrapolation using only $N_t = 4, 6$ from the data in [30] would give a larger T_c than using the full data set. On the other hand, comparing the results obtained from the analysis of Polyakov loops between the two works gives only a small discrepancy. Clearly, cross checks with higher precision, more lattice spacings and other fermion discretizations are needed in order to come to fully conclusive results for the continuum. This discussion elucidates the difficulty of extracting accurate continuum information from lattice data, when statistical errors only appear to be small and under control.

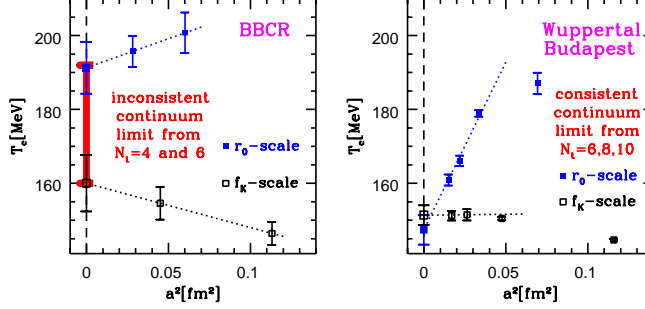


Fig. 3. Left: Reanalysis of the data from [29] with different ways of setting the scale. Right: Same for the data from [30]. Both plots from [30].

3.2 The equation of state

Energy density $\epsilon(T)$ and pressure $p(T)$ as a function of temperature are certainly among the most fundamental thermodynamic quantities of QCD governing, *e.g.*, the expansion of the plasma in the early universe as well as in heavy ion collisions. The partition function for gases of free fermions and bosons are known exactly, and we recall the results in the relativistic and non-relativistic limits, the former corresponding to the famous Stefan-Boltzmann result:

$$\begin{array}{ll}
 \text{Relativistic Boson, } m \ll T & \times \text{ (Fermion) Non-relativistic, } m \gg T \\
 p_r = g \frac{\pi^2}{90} T^4 & \left(\frac{7}{8} \right) \quad p_{nr} = g T \left(\frac{mT}{2\pi} \right)^{\frac{3}{2}} \exp(-m/T) \\
 \rho_r = g \frac{\pi^2}{30} T^4 & \left(\frac{7}{8} \right) \quad \rho_{nr} = \frac{m}{T} p_{nr} \gg p_{nr}
 \end{array} \quad (20)$$

For the fully interacting case, we need to compute the free energy density $f = -T/V \ln Z(V, T)$ of the QCD partition function, and the pressure follows as $p = -f$. A technical obstacle here is that, in a Monte Carlo simulation, one cannot compute the partition function directly, since that provides the probability weights and is normalized to one. What one can compute are expectation values $\langle O \rangle$. The most frequently used detour is called the integral method [31], which computes a suitable derivative of the free energy resulting in a non-trivial expectation value, and then integrates the result,

$$\left. \frac{f}{T^4} \right|_{\beta_0}^{\beta} = -\frac{N_t^4}{V N_t} \int_{\beta_0}^{\beta} d\beta' \left(\left\langle \frac{\partial \ln Z}{\partial \beta'} \right\rangle - \left\langle \frac{\partial \ln Z}{\partial \beta'} \right\rangle_{T=0} \right). \quad (21)$$

Note that this introduces a lower integration constant, which needs to be fixed for the result to be meaningful. While we do not know $f(\beta_0)$ from first principles, we can choose β_0 corresponding to a temperature below the phase transition, where the free energy should be well modelled by a weakly interacting glueball gas. Glueballs are heavy ($\gtrsim 1.6$ GeV), and according to eq. (20) they produce exponentially small pressure which can be approximated by zero.

Another difficulty is that strong discretization effects are to be expected. At high temperature the relevant partonic degrees of freedom have momenta of order $\pi T \sim \pi/(aN_t)$, *i.e.* on the scale of the lattice spacing, which thus strongly affects them. For the equation of state it is therefore particularly important to gain control over these effects and carry out the continuum limit $a \rightarrow 0$. This motivates the use of improved actions, designed to minimize cut-off effects in the approach to the continuum.

The results of a computation of the pressure with an improved action [32] are shown in fig. 4. The data have been obtained for $N_f = 2, 3$ with (bare) mass $m_q/T = 0.4$ as well as for $N_f = 2 + 1$ with a heavier mass $m_q/T = 1$. For comparison the figure includes the continuum extrapolated pure gauge result. The figure shows a rapid rise of the pressure in the transition region. The critical temperature as well as the magnitude of p/T^4 reflect the number of degrees of freedom liberated at the transition. This last conclusion is firm, since the pressure also rises

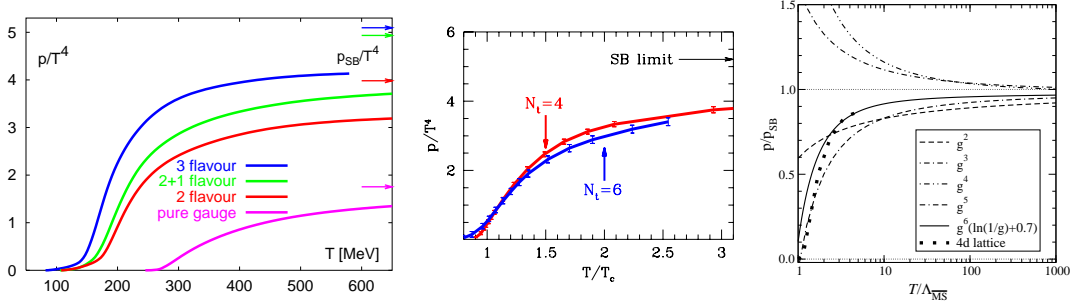


Fig. 4. Left: Flavour dependence of the pressure for $N_t = 4$ lattices compared to a continuum extrapolated pure gauge result. From [32]. Middle: The pressure for $N_f = 2 + 1$ with physical quark masses on $N_t = 4, 6$. From [33]. Right: Various orders of perturbation theory and computation within the 3d effective field theory to order $g^6 \ln(1/g)$. A missing contribution to $O(g^6)$ has been adjusted by matching to the 4d lattice results, represented by the diamonds. From [35].

for fixed temperature when light quarks are added to the theory, consistent with the behaviour in the Stefan-Boltzmann limit.

An important question then is whether these features survive in the continuum limit. Again, in pure gauge theory this can be firmly established by numerical extrapolation. First steps towards a continuum extrapolation of dynamical simulations have been taken in [33,34], with consistent results. An example is shown in fig. 4 (middle), which was computed with bare quark masses tuned to their physical values. The trend to fall short of the Stefan-Boltzmann limit turns out to be confirmed on a finer lattice, and hence appears to be a robust result about the quark gluon plasma at moderate temperatures.

Investigations of the equation of state thus provide us with an intriguing picture of the complexity of the quark gluon plasma. The sudden rise in pressure across the critical temperature has to be interpreted as a release of degrees of freedom, and in this sense it is justified to speak of a deconfining transition. On the other hand, the deconfined phase clearly shows remnant interactions and the released degrees of freedom are not appropriately characterized as a nearly free parton gas.

At asymptotically high temperatures, the pressure eventually must meet the free gas limit because of asymptotic freedom. This can be studied in the framework of the dimensionally reduced effective high T theory. The pressure can be computed perturbatively to the order g^5 before the prohibitive Linde problem sets in at $O(g^6)$ [4]. Fig. 4 (right) shows the poor convergence behaviour of the series up to that order. The non-perturbative g^6 contribution is dominated by the magnetic modes $\sim g^2 T$. However, it can be computed on the lattice by simulations of the 3d effective high temperature theory [36]. This requires matching of the coefficients between the effective and the full theory and converting from lattice to $\overline{\text{MS}}$ regularization schemes at four loop level, a task that has been recently completed [37]. However, there is one last missing contribution to $O(g^6)$ coming from the perturbative scale $\sim T$. In the figure this coefficient has been chosen such that the results for the pressure computed in this framework match on to the lattice results at lower temperatures.

3.3 Screening masses

Essentially all static equilibrium properties of a thermal quantum field theory are encoded in its equal time correlation functions. These are quantities that are well defined and calculable to good precision by lattice methods. Unfortunately, these quantities are not directly accessible in heavy ion collision experiments. Nevertheless, their theoretical knowledge provides us with the relevant length scales in the plasma, from which conclusions about the active degrees of freedom and their dynamics may be drawn. The connected spatial correlation functions of gauge-invariant, local operators $A(x)$,

$$C(|\mathbf{x}|) = \langle A(\mathbf{x})A(0) \rangle_c \sim e^{-M|\mathbf{x}|}, \quad (22)$$

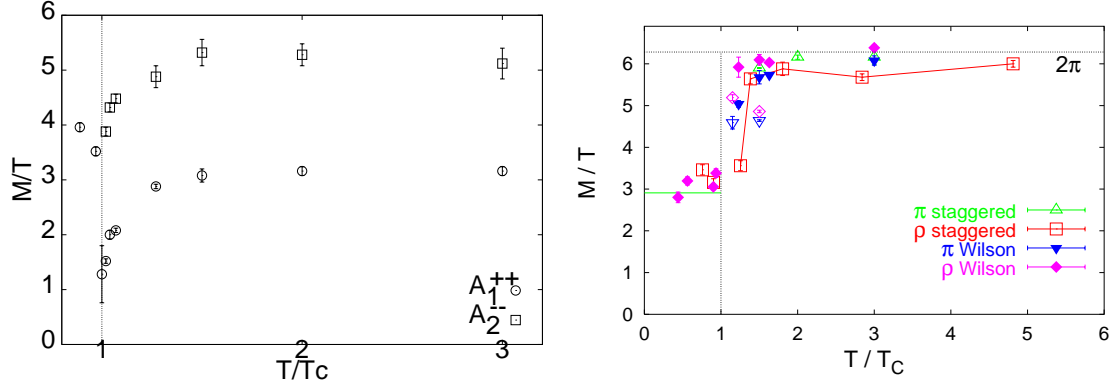


Fig. 5. Left: Screening masses for the pure gauge theory from $N_t = 4$ lattices, corresponding to the continuum 0_{++}^{++} (circles) and 0_{+-}^{+-} (squares) channels. From [41]. Right: Mesonic screening masses in the quenched chiral limit. Below T_c , M_ρ/T_c [42] is plotted, the line denotes the $T = 0$ value. Open Wilson symbols denote anisotropic lattices [43]. Staggered pion data are extrapolated to $a = 0$ [44], Wilson and staggered rho are from $N_t = 8$ [42] and 16 lattices. The free quark limit has not been corrected for finite volume effects. From [26].

fall off exponentially with distance. The “screening masses” M are the eigenvalues of the space-wise Hamiltonian of the corresponding lattice field theory, and classified by its symmetries. Because of the shortening of the euclidean time direction at $T > 0$, the continuum rotation symmetry of the hypertorus orthogonal to the correlation direction is broken down from $O(3)$ to $O(2) \times Z(2)$, and its appropriate subgroup for the lattice theory is D_h^4 . The irreducible representations and the classification of operators have been worked out for pure gauge theory [38,39] as well as for staggered quarks [40]. Physically, the screening masses correspond to the inverse length scale over which the equilibrated medium is sensitive to the insertion of a static source carrying the quantum numbers of A . Beyond $1/M$, the source is screened and the plasma appears undisturbed. Technically, the computation of these quantities is equivalent to spectrum calculations at zero temperature.

Fig. 5 (left) shows results for the lowest lying screening masses corresponding to glue-ball operators around T_c . In the range $0.8T_c < T < T_c$, the lowest scalar screening mass is observed to be roughly 20% lower than the lightest scalar glueball at zero temperature, $M(T)/M_G(T=0) \sim 0.8$. At T_c a sharp dip is observed, after which the screening masses appear to be proportional to T . Screening states with larger masses show the same qualitative behavior above T_c .

Apart from pure glue operators A in eq. (22), also correlations of meson operators have been investigated, both in the quenched approximation as with various numbers of dynamical fermions. The picture which has emerged so far is illustrated by some of the available data shown in fig. 5 (right). Below T_c , the screening masses do not show a marked temperature dependence and roughly agree with the corresponding zero temperature masses. At temperatures (slightly) above T_c spatial (as well as temporal) correlation functions reflect the restoration of the chiral $SU_L(N_f) \times SU_R(N_f)$ symmetry. In particular, the vector and axial vector channel become degenerate independent of the discretization and of the number of dynamical flavors being simulated. Moreover, the pion ceases to be a Goldstone boson and acquires a screening mass.

At sufficiently high temperature, the screening masses are expected to approach the limit of freely propagating quarks, $M \rightarrow 2\pi T$. In fact, already at temperatures of about $1.5 T_c$, the results for the vector channel are not far from this value. If the finite volume effects for free quark propagation are taken into account, the deviations amount to about 15 % and decrease slowly with temperature. Thus, the hard fermionic modes $\sim \pi T$ behave quasi-perturbatively. Quenching effects are found to be below 5% for $T > T_c$ [45], so the computer time saved on dynamical fermions can be invested in finer lattices and results are close to continuum physics.

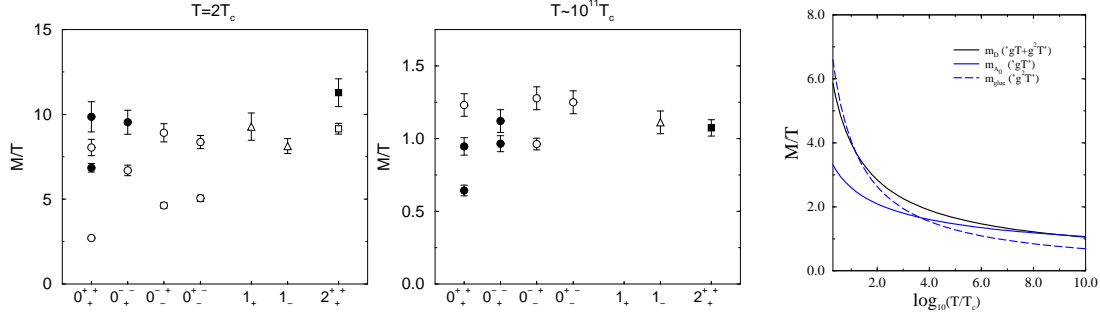


Fig. 6. Pure gauge screening masses from simulations of the effective 3d theory in various quantum number channels for $T = 2T_c$ (left) and $T = 10^{11}T_c$ (middle). Filled symbols refer to operators made of only magnetic gauge fields $A_i \sim g^2T$, while open symbols also contain electric gauge fields $A_0 \sim gT$. From [21]. Right: Interpolated temperature dependence of the two lowest 0_+^{++} and the lowest 0_-^{++} states [46].

In the plasma phase, screening masses can also be investigated within the dimensionally reduced theory, cf. section 2.6. In this framework they correspond to the spectrum of the transfer matrix for the 3d theory. The associated Hamiltonian respects $SO(2)$ planar rotations, two-dimensional parity P , A_0 -reflections R , and the symmetry is again $SO(2) \times Z(2) \times Z(2) = O(2) \times Z(2)$. Remember, however, that in this setup one is interested in soft modes, while the Matsubara frequency $\sim 2\pi T$ represents the UV cut-off for the effective theory.

The approach of dimensional reduction is particularly valuable in disentangling contributions from different degrees of freedom by accurate mixing analyses, as well as for treating larger temperatures $T \gg T_c$ which cannot be reached by 4d lattices. This can be used to inspect to what extent the plasma behaves perturbatively. fig. 6 then tells us that for any experimentally accessible temperature the largest correlation length of gauge-invariant operators belongs to the $A_0 \sim gT$ degrees of freedom and not to the $A_i \sim g^2T$, in contrast to the naive parametric ordering eq. (16). Only asymptotically is the perturbative ordering restored. Thus, on the soft scales $\sim gT$ and $\sim g^2T$ the plasma is strongly coupled.

3.4 The free energy of static quarks

The free energy of a static quark-antiquark pair is of interest for the physics of heavy quarkonia in the medium, and in particular to the question of J/ψ -suppression due to screening of the confining potential [47]. Potential models are then used to study bound state solutions, suitably generalized to finite temperature. More refined treatments try to establish a connection between the static potential and quarkonium spectral functions, to be discussed in the next section. Non-perturbative free energies serve as input for such applications, for recent work and references, see [48].

The $q\bar{q}$ free energy is defined [14] by the partition function of the thermal heat bath containing a static quark and antiquark source at separation \mathbf{r} ,

$$\langle \text{Tr} L(\mathbf{r}) \text{Tr} L^\dagger(0) \rangle = \exp\{-(F_{q\bar{q}}(|\mathbf{r}|, T) - F_0(T))/T\}, \quad (23)$$

where F_0 denotes the free energy of the heat bath. At zero temperature, *i.e.* $N_t \rightarrow \infty$, $F_{q\bar{q}}$ reduces to the static quark potential.

Let us begin our discussion in the pure gauge limit, where the expectation value of the Polyakov loop is a true order parameter. Numerical results below and above the pure gauge phase transition are given in [49]. When the temperature is switched on and increased towards T_c , a linearly rising free energy is maintained, implying infinite energy cost in separating the quark infinitely from the anti-quark, and thus confinement. However, the slope decreases with

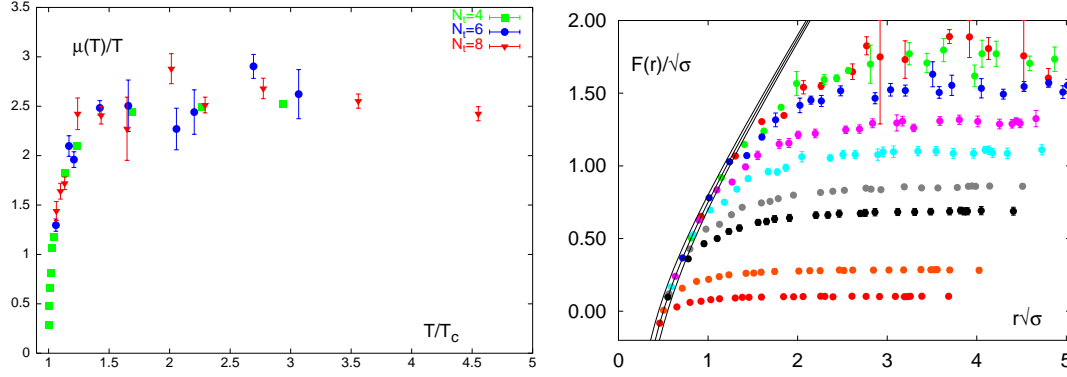


Fig. 7. Left: Screening mass (quenched) for $T > T_c$ from fits to eq. (25), $d = 3/2$ [49]. Right: Static quark free energy for $N_f = 3$ at temperatures $0.58 < T/T_c < 1.15$ [53]. $F(r)$ is normalized at $(r = 1/T)$ to the $T = 0$ Cornell potential, $V(r)/\sqrt{\sigma} = -\alpha/r\sqrt{\sigma} + r\sqrt{\sigma}$ with $\alpha = 0.25 \pm 0.05$ (solid band).

temperature, and the corresponding effective string tension is well fitted by the form

$$\frac{\sigma(T)}{\sigma(0)} = a \sqrt{1 - b \frac{T^2}{T_c^2}}, \quad (24)$$

(predicted by an effective Nambu-Goto string [50]), with $a = 1.21(5)$ and $b = 0.990(5)$ [49]. Above T_c an exponentially screened free energy is obtained, fitting an ansatz of the form

$$\frac{F_{q\bar{q}}(r, T)}{T} = -\frac{e(T)}{(rT)^d} e^{-\mu(T)r}. \quad (25)$$

In perturbation theory, the leading term originates from two-gluon exchange and predicts $d = 2$ and exponential decay with twice the Debye mass [51]. Lattice investigations [49,52] have shown that this simple behavior does not apply in the temperature and distance range explored. Rather, fits [49] to eq. (25) favoured $d \simeq 3/2$ and found screening masses $\mu(T)$, shown in fig. 7 (left), to be compatible with the lowest color singlet 0_{++}^{++} screening mass shown in figs. 5, 6. This is not surprising: the Polyakov loop is a gauge invariant operator, and since it is an exponential of gauge fields it couples to all J^{PC} sectors. Consequently, its correlator decays with the lightest screening mass of the spectrum.

When dynamical light quarks are present, the color charges of the heavy quarks are screened also below T_c and one observes [53,54,55] the expected string breaking, fig. 7 (right). The distances where the free energies become flat in r range from 1.5 to 1 fm, decreasing with temperature, even at (bare) quark masses as large as $m/T = 0.4$. Note that the deviations from the zero temperature quenched potential set in already at distances of $\mathcal{O}(0.5\text{fm})$ for temperatures $\gtrsim 0.75T_c$. When the free energy is normalized to the short distance zero temperature potential, its large r asymptotic value rapidly decreases with T .

The gauge invariant Polyakov loop averages over color singlet and octet configurations of the static source. Correspondingly, its correlator is often written as a superposition [14,51,56]

$$e^{-F_{q\bar{q}}(r,T)/T} = \frac{1}{9} e^{-F_1(r,T)/T} + \frac{8}{9} e^{-F_8(r,T)/T}, \quad (26)$$

with singlet and octet channels defined as

$$\begin{aligned} e^{-F_1(r,T)/T} &= \frac{1}{3} \langle \text{Tr } L^\dagger(\mathbf{x}) L(\mathbf{y}) \rangle, \\ e^{-F_8(r,T)/T} &= \frac{1}{8} \langle \text{Tr } L^\dagger(\mathbf{x}) \text{Tr } L(\mathbf{y}) \rangle - \frac{1}{24} \langle \text{Tr } L^\dagger(\mathbf{x}) L(\mathbf{y}) \rangle. \end{aligned} \quad (27)$$

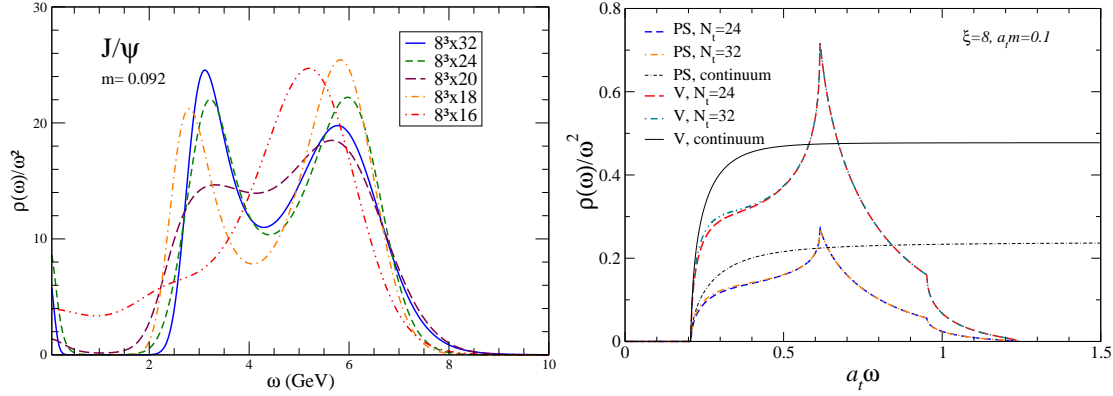


Fig. 8. Left: Spectral function in the vector channel for different temperatures on $8^3 \times N_t$ lattices, [62]. Right: Free fermion spectral functions in the pseudo-scalar and vector channels, [63].

While the singlet correlator is obviously gauge-dependent, the energy eigenvalues governing its decay in a spectral analysis are not [57] and one might hope to gain useful insight into the colour dynamics to be used in potential models. However, this is dangerous. A careful spectral expansion making use of projection operators on the representations reveals that both, the singlet and the octet channel, decay as $\sim \sum_n |c_n[U]|^2 \exp(-E_n/T)$ [58], where the energies E_n represent the same static potential and its excitations which also contribute to the “average” free energy, while the matrix elements $c_n[U]$ depend on the gauge or the operator used to describe the spatial string. Thus, the gauge-invariant spectral information is the same for all channels, while F_1, F_8 and their difference from $F_{q\bar{q}}$ are properties of the operators used, leaving their physical meaning in doubt.

3.5 Dynamical quantities: quarkonium spectral functions and transport coefficients

Quarkonium physics in the plasma can also be formulated more rigorously in a quantum field theoretical way. The physical excitations of the plasma with a given set of quantum numbers are encoded in the retarded Green’s functions, or real time correlators, of operators carrying those quantum numbers [3]. In general the poles of such (momentum space) Green’s functions will be complex, thus they are *not* eigenvalues of the Hamiltonian. If the imaginary part is small compared to the real part, one speaks of a quasi-particle excitation, with the real part interpreted as its mass and the imaginary part as its decay width, due to Landau damping in the plasma.

Unfortunately, Monte Carlo methods only work for euclidean actions, and direct numerical simulations of real time correlators are impossible. However, one may try to statistically exploit the information encoded in euclidean Green’s function as follows. Let $G_\Gamma(\tau) = \sum_{\mathbf{x}, \mathbf{y}, t} \langle \bar{\psi}(\mathbf{x}, t) \Gamma \psi(\mathbf{x}, t) \bar{\psi}(\mathbf{y}, t + \tau) \Gamma \psi(\mathbf{y}, t + \tau) \rangle$ be a correlator of some meson operator in euclidean time. Then its Fourier transform is given by

$$G_\Gamma(\tau, \mathbf{p}) = \int_0^\infty \frac{d\omega}{2\pi} \rho_\Gamma(\omega, \mathbf{p}) K(\tau, \omega), \quad K(\tau, \omega) = e^{\omega\tau} n_B(\omega) + e^{-\omega\tau} [1 + n_B(\omega)], \quad (28)$$

where all the time dependence resides in the kernel $K(\tau, \omega)$, which contains only thermal distribution functions. All the dynamical, spectral information of the theory is contained in $\rho(\omega, \mathbf{p})$, which will not change under analytic continuation to Minkowski time. Still the difficulties are formidable. Computing G_Γ by lattice simulations, the left hand side is given only by a finite number of points and the inversion of the integral is an ill-defined problem. The way out is to “guess” with statistical methods the most likely $\rho(\omega, \mathbf{p})$ which will fit the formula. This is known as maximum entropy method (MEM), whose details are explained in [59]. Clearly, one needs as many points in the time direction as possible, hence anisotropic lattices with $a_t \ll a_s$

are useful. Another problem is that the MEM needs a prior, *i.e.* a model function has to be provided to constrain the fitted function. Usually one models spectral functions perturbatively at large ω . For a discussion of this and other systematic difficulties, see [60].

Early results based on this approach, obtained with quenched simulations, indicated that J/ψ does not melt up to temperatures of $1.5 - 2T_c$ [61], thus providing another reason to term the QGP ‘strongly coupled’. There are now also dynamical simulations confirming this picture, as shown in fig. 8 (left) for $N_f = 2$ [62]. The temperatures parametrized by the shown N_t ’s correspond to $T_c - 2T_c$. At low temperatures, the position of the first peak corresponds to the zero temperature mass of the J/ψ . As temperature increases, the peak shrinks but keeps existing until about $1.7T_c$, when it finally disappears. Hence the conclusion that “ J/ψ doesn’t melt” until then (for another interpretation see [48]). No physical meaning can be attributed to the second peak, which is interpreted as a lattice-distorted part of the free particle continuum. This is illustrated in fig. 8 (right), where the spectral function for free particles in the scalar and vector channel are plotted in the continuum and on the lattice. The finite cut-off is faking a peak, which should disappear in the continuum limit.

Other quantities of tremendous phenomenological interest are transport coefficients. In particular, the shear viscosity is defined as the slope of another spectral function,

$$\eta = \frac{1}{20} \frac{d}{d\omega} \rho_{\pi\pi}(\omega) \Big|_{\omega=0}, \quad G_{\pi\pi}(\tau) = \int d^3x \langle \pi_{kl}(\tau, \mathbf{x}) \pi_{kl}(0, \mathbf{0}) \rangle = \int \frac{d\omega}{2\pi} K(\tau, \omega) \rho_{\pi\pi}(\omega), \quad (29)$$

where π_{kl} is the traceless part of the spatial energy-momentum tensor. The numerical procedure to compute this on a lattice is the same as above. Here accurate information, and hence high resolution, on the low frequency tail is required. An early numerical attempt [64] as well as a recent more refined analysis [65] for the pure gauge theory give small viscosity to entropy ratios, $\eta/s \sim 0.1 - 0.2$, consistent with observations in the quark gluon plasma. However, it has been pointed out that extracting the low frequency part is firstly sensitive to modelling the spectral function [60], and second intrinsically unstable, though this problem could be removed by a simple rescaling trick [66]. Building on this, ref. [65] suggested a new method to systematically improve on the spectral function by expanding it in terms of an orthogonal function system and fitting its coefficients. Hence, MEM calculations might soon offer some control over systematics.

Finally, a different approach to compute spectral functions is currently emerging, generalizing heavy quark effective field theory methods to real time correlation functions at finite temperature [67]. In the heavy quark limit a certain meson correlator reduces to a Wilson loop in Minkowski time. Thus, the static potential reappears in a real time framework, but it develops an imaginary part which is responsible for the damping and melting of the bound state [67]. It has been shown in HTL perturbation theory that indeed a broadening spectral function is obtained in this approach [68]. The imaginary part of the potential has recently been confirmed non-perturbatively by classical lattice simulations [69]. It will be interesting to see if this approach can be generalized to the full quantum theory in the future, thus providing a bridge between field theory and potential models.

4 The nature of the QCD phase transition

In the previous sections we discussed the properties of QCD matter on either side of the quark hadron transition, but haven’t yet addressed what the nature of that transition is. To obtain an unambiguous answer to this question is in fact a very difficult task. In statistical mechanics, phase transitions are defined as singularities, or non-analyticities, in the free energy as a function of its thermodynamic parameters. However, on finite volumes, free energies are always analytic functions and it can be proved that singularities only develop in the thermodynamic limit of infinitely many particles, or $V \rightarrow \infty$ [70]. This is particularly obvious in the case of lattice QCD, whose partition function is a functional integral over a compact group with a bounded exponential as an integrand. It is thus a perfectly analytic function of T, μ, V for any finite V . Hence, a theoretical establishment of a true phase transition requires finite size scaling (FSS) studies on a series of increasing and sufficiently large volumes in order to extrapolate to

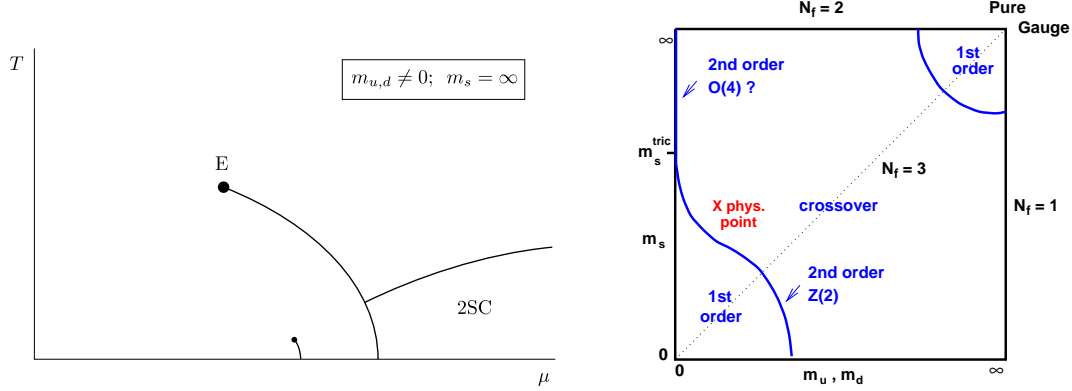


Fig. 9. Left: Conjectured phase diagram for $N_f = 2$ QCD with finite light quark masses. The physical case $N_f = 2 + 1$ is believed to qualitatively look the same, according to universality and continuity arguments as well as results from QCD-like models [2]. Right: Schematic phase transition behaviour of $N_f = 2 + 1$ flavor QCD at $\mu = 0$ for different choices of quark masses $(m_{u,d}, m_s)$, at $\mu = 0$.

the thermodynamic limit. Three different situations can emerge: a first order phase transition is characterized by coexistence of two phases, and hence a discontinuous jump of the order parameter (and other quantities) when going through such a transition. A second order transition shows a continuous transition of the order parameter accompanied by a divergence of the correlation length and some other quantities, like the heat capacity. Finally, a marked change in the physical properties of a system may also occur without any non-analyticity of the free energy, in which case it is called an analytic crossover. A familiar system featuring all these possibilities is water, with a weakening first order liquid-gas phase transition terminating in a critical endpoint with $Z(2)$ universality, as well as a triple point where the first order liquid-gas and solid-liquid transitions meet. Similar structures are also conjectured to be present in the QCD phase diagram [2,71], fig. 9 (left). In this section we focus on the order of the transition for $\mu = 0$ as a function of N_f and quark masses, before tackling $\mu \neq 0$ in sec. 5.

4.1 Universality and finite size scaling

A most fascinating phenomenon in physics is the “universality” exhibited by physical systems near a critical point of second order phase transition. It is due to the divergence of the correlation length, which implies that the entire system acts as a coherent collective. Hence, microscopic physics becomes unimportant, the collective behaviour is determined by global symmetries. With the divergence of the correlation length the characteristic length scale disappears from the problem, and thermodynamic observables in the critical region obey scale invariant power laws. For example, at a second order ferromagnetic phase transition, the order parameter magnetization vanishes as $M \sim |T - T_c|^\beta$, while the specific heat and correlation length diverge, $C \sim |T - T_c|^{-\alpha}$ and $\xi \sim |T - T_c|^{-\nu}$, respectively. The critical exponents α, β, ν and similar ones for other quantities are determined by the effective global symmetries at the critical point, and thus are the same for all systems within a universality class. The latter are labeled by spin models, since those can be readily solved numerically. The power law behaviour for thermodynamic functions follows from the scaling form of the singular part of the free energy,

$$f_s(t, h) = L^{-3} f_s(L^{y_t} \tau, L^{y_h} h), \quad (30)$$

where L denotes the box size, and τ and h are the relevant scaling fields. In the case of the Ising model these are the reduced temperature and magnetic field. Unfortunately, for most systems, and particularly QCD, it is not obvious which global symmetries the system will exhibit at a critical point, those are a dynamically determined subset of the total symmetry of the theory. Moreover, since there is no true order parameter in the case of finite quark masses, fields and parameters of QCD map into those of the effective model in a non-trivial way.

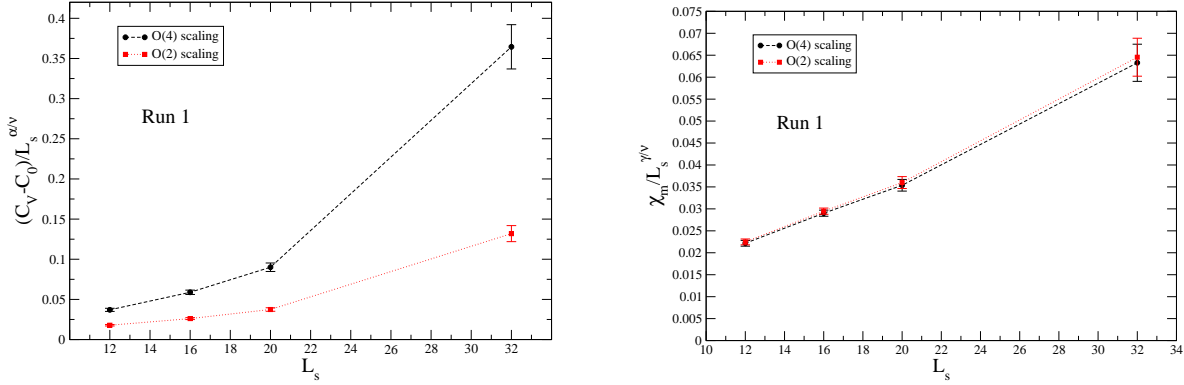


Fig. 10. Finite volume scaling behaviour of specific heat and chiral susceptibility on $N_t = 4$. For O(4) viz. O(2) behaviour, the data should fall on a horizontal line [76].

4.2 The nature of the QCD phase transition for $N_f = 2 + 1$ at $\mu = 0$: qualitative picture

Before discussing numerical results, let us briefly outline the qualitative picture for the order of the phase transition, fig. 9 (right). As mentioned in sec. 2.5, for $N_f = 3$ in the limits of zero and infinite quark masses (lower left and upper right corners), order parameters corresponding to the breaking of a symmetry can be defined, and one finds numerically at small and large quark masses that a first-order transition takes place at a finite temperature T_c . On the other hand, one observes an analytic crossover at intermediate quark masses. Hence, each corner must be surrounded by a region of first-order transition, bounded by a second-order line. The situation is less clear for the chiral limit of the two flavour theory in the upper left corner. If the transition is second order, then chiral symmetry $SU_L(2) \times SU(2)_R \sim O(4)$ puts it in the universality class of 3d $O(4)$ spin models. In this case there must be a tricritical strange quark mass m_s^{tric} , where the second order chiral transition ends and the first order region begins. The exponents at such a tricritical point would correspond to 3d mean field [71]. On the other hand, a first order scenario for the chiral limit of $N_f = 2$ is a logical possibility as well.

4.3 The chiral transition for $N_f = 2$: is it O(4) or first order?

On the lattice, O(4) will effectively look like O(2) as long as there are discretization effects [72]. Wilson fermions appear to see O(4) scaling [73], while staggered actions are inconsistent with both O(4) and O(2) [74]. (The staggered strong coupling limit, however, does display O(2) scaling [75]). An attempt to tackle this question by means of a finite size scaling analysis with unprecedented lattice sizes was made in [76]. The work simulates $L^3 \times 4$ lattices with $L = 16 - 32$, using standard staggered fermions with several quark masses, the smallest being $m/T \lesssim 0.055$. In a critical region, the specific heat or the chiral susceptibility scale as

$$\begin{aligned} C_V - C_0 &\simeq L^{\alpha/\nu} f_c \left(\tau L^{1/\nu}, am L^{y_h} \right), \quad \tau = 1 - T/T_c \\ \chi &\simeq L^{\gamma/\nu} f_\chi \left(\tau L^{1/\nu}, am L^{y_h} \right). \end{aligned} \quad (31)$$

Here the non-singular part of the specific heat C_0 has been subtracted. The authors of [76] thus fix y_h to its critical value, and then choose L and m for a series of simulations such as to keep $(am L^{y_h})$ constant, reducing the scaling problem on one variable only. The infinite volume limit in this procedure thus corresponds to the chiral limit and allows to check whether the data are consistent with the predicted scaling behaviour.

Fig. 10 shows simulation results from [76]. Scaling as in eq. (31) would imply the data points to fall on a horizontal line, which is clearly not the case. After many variations on the analysis, the authors conclude that their data are closer to first order behaviour than to O(4)/O(2).

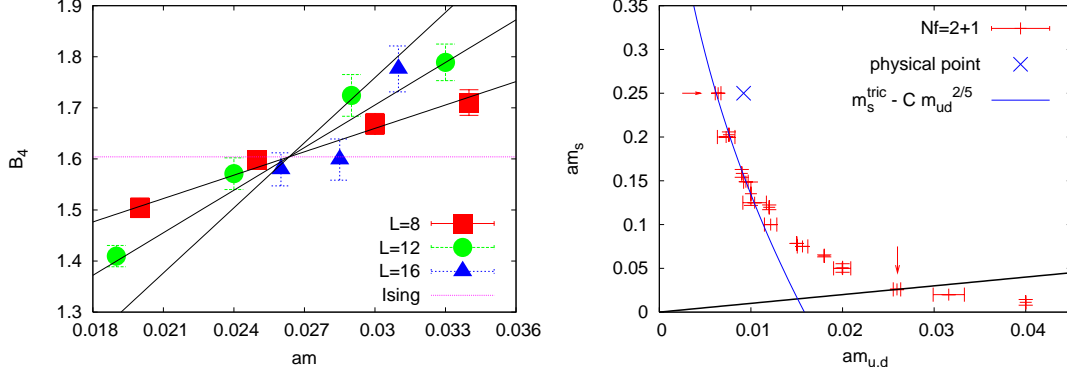


Fig. 11. Left: The Binder cumulant as a function of quark mass for $N_f = 3, N_t = 4$ and different lattice sizes [82]. Right: The chiral critical line in the bare quark mass plane at $\mu = 0, N_t = 4, N_f = 3$ is indicated by the solid line. Also shown are the physical point according to [85], and an extrapolation using mean field exponents to the chiral limit, giving $m_s^{\text{tric}} \sim 2.8T$. The point marked by the arrow has $m_\pi/m_\rho = 0.148(2)$, compared to the physical value 0.18. From [82].

A different conclusion was reached in [77], in which χ QCD was investigated numerically. This is a theory modified by an irrelevant term (*i.e.* one going to zero in the continuum limit) such as to allow simulations in the chiral limit. The authors compare their data with those obtained from an $O(2)$ spin model on moderate to small volumes and find them to be compatible. This might point at finite volume effects of current $N_f = 2$ QCD simulations. The scaling region of the chiral limit might be excessively small, which would require extraordinarily large volumes in order to see the correct scaling. Another possibility for the failure of simulations to unambiguously pin down the order of this transition is of course the failure of the fermion discretizations to reproduce chiral symmetry. Future studies on either finer lattices or with chiral fermion actions should help to clarify this issue.

Another possibility is to study the strength of the $U_A(1)$ anomaly discussed in sec. 2.5, which also enters the effective sigma model [16] for the critical region. It has recently been non-perturbatively demonstrated that a strong anomaly is required for the chiral phase transition to be second order [78].

4.4 $N_f = 2 + 1$: 3d Ising universality and the critical line $m_s^c(m_{u,d})$

Next we move our attention to the second order boundary line separating the first order region from the crossover in fig. 9 (right), starting with degenerate quark masses, $N_f = 3$. In this case on $N_t = 4$ lattices the critical quark mass marking the boundary between the crossover and the first order region is large enough for simulations to be carried out, and it was possible to determine it quite accurately [79,80,81,82], together with the $Z(2)$ universality class of the 3d Ising model to which it belongs [79]. The most practical observable to determine the latter is the Binder cumulant, constructed from moments of fluctuations of the order parameter,

$$B_4(m, \mu) = \frac{\langle (\delta\bar{\psi}\psi)^4 \rangle}{\langle (\delta\bar{\psi}\psi)^2 \rangle^2}, \quad \delta\bar{\psi}\psi = \bar{\psi}\psi - \langle \bar{\psi}\psi \rangle, \quad (32)$$

evaluated on the phase boundary $\beta = \beta_c(m, \mu)$. In the infinite volume limit, $B_4 \rightarrow 1$ or 3 for a first order transition or crossover, respectively, whereas it approaches a value characteristic of the universality class at a critical point. For 3d Ising universality one has $B_4 \rightarrow 1.604$ [83]. Hence B_4 is a non-analytic step function, which gets smoothed out to an analytic curve on finite volumes, with a slope increasing with volume to gradually approach the step function.

A numerical example is shown in fig. 11 (left). The slope increases with lattice size, and the data fit the finite volume scaling formula predicted by universality,

$$B_4(m, L) = b_0 + bL^{1/\nu}(am - am^c). \quad (33)$$

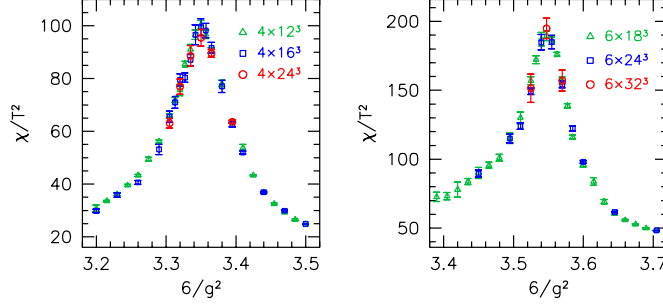


Fig. 12. Finite size scaling of the chiral susceptibility at the physical point for two lattice spacings $N_t = 4$ (left) and $N_t = 6$ (right). The peaks saturate at a finite height, consistent with an analytic crossover.

One observes that all curves intersect at the critical B_4 -value, and moreover ν is consistent with its 3d Ising value $\nu = 0.63$. Hence we can read off the critical quark mass in lattice units, $am^c = 0.0263(3)$ or $m^c/T_c = 1.052(1)$ [82].

While the nature of the transition and its universality class are determined by long range fluctuations and thus should be insensitive to the cut-off effects on a coarse lattice, the critical quark mass is a quantity requiring renormalization and is tremendously sensitive to such effects. Indeed, the critical quark mass and the corresponding pion mass have been computed on $N_t = 4$ lattices with a standard staggered and a p4-improved staggered action. The critical pion mass in the improved case is almost a factor of four smaller than the non-improved result [79,34]. Hence, the location of the boundary line in the phase diagram is still far from the continuum result.

Starting from the critical quark mass for $N_f = 3$, the boundary line has also been mapped for the non-degenerate $N_f = 2 + 1$ theory, again with $N_t = 4$ [82]. The question now arises which flavours to couple to the quark chemical potential. Within QCD alone there are no flavour changing interactions, while the initial state in heavy ion collisions has net u, d -quark numbers only. Thus it is sensible to assign a chemical potential to the two degenerate light quarks only. In nature, where the weak interactions are switched on as well, the situation is somewhat more complicated than this [84]. The methodology then is the same as in the three flavour case: fix a strange quark mass am_s and scan the Binder cumulant in the light quark mass $am_{u,d}$ for the corresponding critical point. Repeating for several strange quark masses produces the critical line $am_s^c(am_{u,d})$ shown in fig. 11 (right). The results are in qualitative agreement with expectations from fig. 9 (right). They are also consistent with the possible existence of a tricritical point ($m_{u,d} = 0, m_s = m_s^{tric}$). Using its known, mean field exponents, the data favour a heavy $m_s^{tric} \sim 2.8T_c$. Again large corrections, presumably towards a smaller value, are expected in the continuum limit. Also, T_c is found to vary little along the critical line, in accordance with model calculations employing effective chiral lagrangians [86].

4.5 The nature of the transition at the physical point

A more immediate issue is whether the QCD physical point indeed lies on the crossover side of the critical line as expected. For that purpose spectrum calculations at $T \sim 0$ have been performed [82] at the parameters indicated by the arrows in fig. 11 (right). They show that m_s at the upper arrow is approximately tuned to its physical value ($\frac{m_K}{m_\rho} \sim \frac{m_K}{m_\rho}|_{\text{phys}} = 0.65$), while the pion is lighter than in physical QCD ($\frac{m_\pi}{m_\rho} = 0.148(2) < \frac{m_\pi}{m_\rho}|_{\text{phys}} = 0.18$). This confirms that the physical point lies to the right of the critical line, *i.e.* in the crossover region.

An important question is whether this finding, calculated on coarse lattices $N_t = 4$, is stable under continuum extrapolations. This has been recently addressed and affirmed in [87], using a Symanzik improved gauge and a stout-link improved staggered fermion action for four different lattice spacings, $N_t = 4, 6, 8, 10$. The simulations were carried out along the lines of

constant physics, *i.e.* the bare parameters were tuned such that the hadron spectrum in physical units is constant for different lattice spacings. The result of a finite size scaling analysis of the susceptibility of the chiral condensate is shown in fig. 12. The peak height appears to clearly saturate at some finite value, and the transition thus corresponds to a crossover. The finite peak height was calculated for all four lattice spacings and extrapolates to a finite value also in the continuum limit. Hence, one concludes that the transition between hadronic and quark gluon plasma physics at zero density indeed is an analytic crossover for physical QCD. In view of the concerns about the validity of the staggered fermion actions [8], it would of course be desirable to reproduce this result with alternative fermion discretizations.

5 Lattice QCD at finite density

Since 2001, significant progress was made towards simulating QCD with realistic parameter values at small baryon densities. This is achieved by a number of methods that circumvent the sign problem, rather than solving it: i) Multi-parameter reweighting, ii) Taylor expansion around $\mu = 0$ and iii) simulations at imaginary chemical potential, either followed by analytic continuation or Fourier transformed to the canonical ensemble. It is important to realize that all of these approaches introduce some degree of approximation. However, their systematic errors are rather different, thus allowing for powerful crosschecks. All methods are found to be reliable as long as $\mu/T \lesssim 1$, or $\mu_B \lesssim 550$ MeV, which includes the region of interest for heavy ion collisions. Reviews specialized on this subject can be found in [88,89].

5.1 Two parameter reweighting

Significant progress enabling finite density simulations was made a few years ago, by a generalization of the Glasgow method [90] to reweighting in two parameters [91]. The partition function is rewritten identically as

$$Z = \left\langle \frac{e^{-S_g(\beta)} \det(M(\mu))}{e^{-S_g(\beta_0)} \det(M(\mu=0))} \right\rangle_{\mu=0, \beta_0}, \quad (34)$$

where the ensemble average is now generated at $\mu = 0$ and a lattice gauge coupling β_0 , while a reweighting factor takes us to the values μ, β of interest. The original Glasgow method [90] reweighted in μ only and was suffering from the overlap problem: while the reweighting formula is exact, its Monte Carlo evaluation is not. The integral gets approximated by a finite number of the most dominant configurations, which are different for the reweighted and the original ensemble, and this difference grows with μ . When searching for a phase transition at some μ , one-parameter reweighting uses a non-critical ensemble at $\mu = 0$, thus missing important dynamics. By contrast, two-parameter reweighting uses an ensemble generated at the pseudo-critical coupling $\beta_c(\mu = 0)$, which is then reweighted along the pseudo-critical line of the phase change. Thus one is working with an ensemble that probes both phases, improving the overlap with the physical ensemble.

A difficulty in this approach is that the determinant needs to be evaluated exactly, which is costly. Moreover, because of the sign problem the reweighting factor is exponentially suppressed with volume and chemical potential, thus limiting the applicability to presently moderate values of those parameters. Moreover, since the statistical fluctuations are those of the simulated ensemble instead of the physical one, all reweighted measurements are correlated and it is difficult to obtain reliable error estimates. For a proposed procedure see [92]. A further problem arises with staggered quarks, where the root of the determinant has to be taken. For $\mu \neq 0$ this may enhance cut-off effects to $O(a)$ instead of $O(a^2)$ for $\mu = 0$ [93].

5.2 Finite density by Taylor expansion

Another way to gain information about non-zero μ is to compute the coefficients of a Taylor series expansion of observables in powers of μ/T . Early attempts have looked at susceptibilities and the response of screening masses to chemical potential [94,95,96,97]. More recently it has also been used to gain information on the phase transition and its nature itself [98,99,100,101,102]. This idea exploits the fact that on finite volumes the partition function $Z(m > 0, \mu, T)$ is an analytic function of the parameters of the theory. For small enough μ/T one may then hope to get away with only a few terms, whose coefficients are calculated at $\mu = 0$. Moreover, because of CP symmetry of the QCD action the partition function is even in μ , $Z(\mu) = Z(-\mu)$, such that physical observables have series expansions in $(\mu/T)^2$. Thus, *e.g.* the pressure density can be expressed as an even power series,

$$p(T, \mu) = -\frac{F}{V} = \left(\frac{T}{V}\right) \log Z(T, \mu), \quad \frac{p}{T^4} = \sum_{n=0}^{\infty} c_{2n}(T) \left(\frac{\mu}{T}\right)^{2n}. \quad (35)$$

The coefficients are equivalent to generalized quark number susceptibilities at $\mu = 0$ and measurable with standard simulation techniques. Since all the μ -dependence of the partition function is in the fermion determinant, its derivatives need to be computed,

$$\frac{\partial \ln \det M}{\partial \mu} = \text{tr} \left(M^{-1} \frac{\partial M}{\partial \mu} \right), \quad \frac{\partial \text{tr} M^{-1}}{\partial \mu} = -\text{tr} \left(M^{-1} \frac{\partial M}{\partial \mu} M^{-1} \right), \quad \text{etc.}, \quad (36)$$

and iterations for higher orders. These expressions become increasingly complex and methods to automatize their generation have been devised [102]. Note that one now is dealing with traces of composite local operators, which greatly facilitates their numerical evaluation by statistical estimators compared to a computation of the full determinant as required for reweighting.

For high enough temperatures $T \gtrsim T_c$, the scale of the finite temperature problem is set by the Matsubara mode $\sim \pi T$, and one would expect coefficients of order one for an expansion in the ‘natural’ parameter $\mu/(\pi T)$ [81]. This is indeed borne out by numerical simulations and explains the good convergence properties observed for $\mu/T \lesssim 1$.

5.3 QCD at imaginary μ

The hermiticity relation eq. (12) tells us that the QCD fermion determinant with imaginary $\mu = i\mu_i$ is real positive, hence it can be simulated just as for $\mu = 0$. It is then natural to ask whether such simulations can be exploited to learn something about physics at real μ . The strategy to get back to real μ is to fit the full Monte Carlo results to a truncated Taylor series in μ_i/T . In case of apparent convergence it is then easy to analytically continue the power series to real μ . This idea was first used for observables like the chiral condensate and screening masses in the deconfined phase [103,96]. It was then shown to be applicable to the phase transition itself [104], which has recently been exploited in a growing number of works [81,82,105,106,107,108,109].

For complex $\mu = \mu_r + i\mu_i$, the QCD partition function eq. (1) is periodic in the imaginary direction, with period $2\pi/N_c$ for N_c colours [110]. Hence, in addition to being even in μ , the partition function has the additional symmetry $Z(\mu_r/T, \mu_i/T) = Z(\mu_r/T, \mu_i/T + 2\pi/3)$. Because of the anti-periodic boundary conditions on fermions, this symmetry implies that a shift in μ_i by certain critical values is equivalent to a transformation by the $Z(3)$ centre of the gauge group. Thus, there are $Z(3)$ transitions between neighbouring centre sectors for all $(\mu_i/T)_c = \frac{2\pi}{3} (n + \frac{1}{2})$, $n = 0, \pm 1, \pm 2, \dots$. It has been numerically verified that these transitions are first order for high temperatures and a smooth crossover for low temperatures [104,105]. This limits the radius of convergence for analytic continuation, which is given by the first such transition, or $\mu/T = \pi/3$. Hence the approach is limited to $|\mu/T| \lesssim 1$.

Within this circle, the strategy then is to measure expectation values of observables at imaginary μ and fit them by a Taylor series,

$$\langle O \rangle = \sum_n c_n \left(\frac{\mu_i}{\pi T} \right)^{2n}. \quad (37)$$

Working at imaginary μ has a couple of technical advantages. It is computationally simple and much cheaper than reweighting or computing coefficients of the Taylor expansion. Moreover, both parameters β, μ are varied and thus one obtains information from statistically independent ensembles. It also offers some control on the systematics by allowing a judgement on the convergence of the fits. Furthermore, it is a good testing ground for effective QCD models: analytic results can always be continued to imaginary μ and be compared with the numerics there, as demonstrated for several examples in [106].

A different approach making use of imaginary chemical potential is to employ the canonical ensemble at fixed quark number, which is related to the grand canonical ensemble via the integral transform

$$Z_C(T, B = 3Q) = \frac{1}{2\pi} \int_{-\pi}^{\pi} d\left(\frac{\mu_i}{T}\right) \exp(-i\mu_i Q/T) Z(\mu = i\mu_i, T, V). \quad (38)$$

One may then compute the grand canonical partition function at imaginary μ and perform the Fourier transform numerically [111]. This will only work for moderate Q and small volumes, as the sign problem is reintroduced by the oscillations of the exponential. For small lattices $6^3 \times 4, 4^4$, first interesting results on the phase diagram have been obtained, both for staggered [112] and Wilson fermions [113]. However, this approach has no overlap problem, and one might hope to push to larger chemical potentials once computational resources are available.

5.4 Plasma properties at finite density

Having developed computational tools for finite density, one can repeat the studies discussed in the previous sections and see how finite baryon densities affect the screening masses [34,95,96,97], the equation of state [100,101,114] or the static potential [115]. In all those cases the influence of the chemical potential is found to be rather weak, and for lack of space we will not further discuss those calculations here. We likewise have to pass over the work done on certain modifications of QCD, for which the sign problem is manageable or absent, such as QCD in the static limit, two-colour QCD or QCD at finite isospin. Such studies give important qualitative insights and some are covered in previous reviews [116,88]. Instead we concentrate here on calculations of the QCD phase diagram at finite density, where the order of the phase transition is expected to change as μ is increased, fig. 9 (left).

5.5 The critical temperature at finite density

As in the case of zero density, let us first discuss the phase boundary, *i.e.* the (pseudo-)critical temperature $T_c(\mu)$, before dealing with the order of the phase transition. The critical line has been calculated for a variety of flavours and quark masses using different methods. For a quantitative comparison one needs data at one fixed parameter set and also eliminate the uncertainties of setting the scale. Such a comparison is shown for the critical coupling in fig. 13 (left), for $N_f = 4$ staggered quarks with the same action and quark mass $m/T \approx 0.2$. (For that quark mass the transition is first order along the entire curve). One observes quantitative agreement up to $\mu/T \approx 1.3$, after which the different results start to scatter. This vindicates our earlier statement that all methods appear to be reliable for $\mu/T \lesssim 1$. Note that strong coupling results at $\beta = 0$ predict $a\mu_c(\beta = 0) = 0.35 - 0.43$ [117], requiring the line to bend down rapidly, and thus favour the data from the canonical approach.

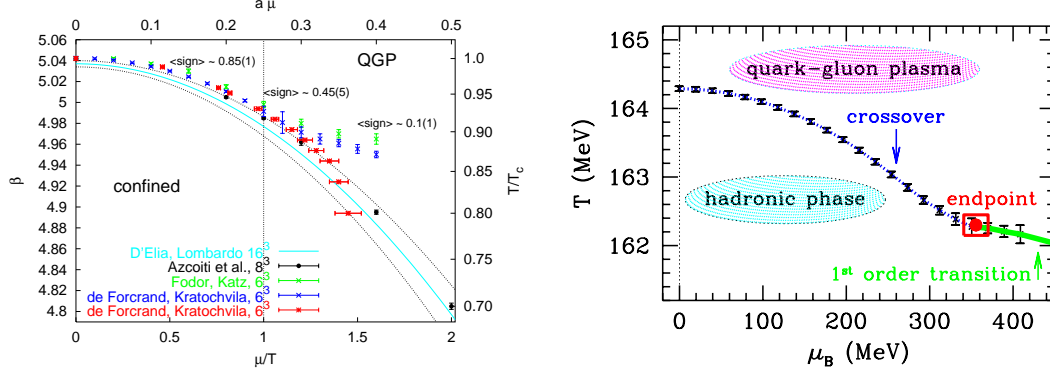


Fig. 13. Left: Comparison of different methods to compute the critical couplings [112]. Right: The phase diagram for physical quark masses as predicted by the two parameter reweighting method [85].

N_f	am	N_s	t_2	Action	β -Function	Method	Reference
2	0.1	16	0.69(35)	p4	non-pert.	Taylor+Rew.	[98]
	0.032	6,8	0.500(54)	stag.	2-loop pert.	Imag.	[104]
3	0.1	16	0.247(59)	p4	non-pert.	Taylor+Rew.	[99]
	0.026	8,12,16	0.667(6)	stag.	2-loop pert.	Imag.	[82]
	0.005	16	1.13(45)	p4	non-pert.	Taylor+Rew.	[99]
4	0.05	16	1.86(2)	stag.	2-loop pert.	Imag.	[105]
2+1	0.0092,0.25	6-12	0.284(9)	stag.	non-pert.	Rew.	[85]

Table 1. Coefficient t_2 in the Taylor expansion of the transition line, eq. (39). All results have been obtained with $N_t = 4$.

The case of physical quark masses, after conversion to continuum units, is shown in fig. 13 (right) [85]. One observes that the critical temperature is decreasing only very slowly with μ . This is consistent with a description by a Taylor expansion in powers of $(\mu/\pi T)^2$ with coefficients of order one,

$$\frac{T_c(\mu)}{T_c(0)} = 1 - t_2(N_f, m_f) \left(\frac{\mu}{\pi T} \right)^2 + \mathcal{O} \left(\left(\frac{\mu}{\pi T} \right)^4 \right) . \quad (39)$$

The leading coefficients for various cases have been collected from the literature in [89] and are reproduced in table 1. The curvature gets stronger with increasing N_f , which is consistent with the observation at zero density that T_c is lowered by light flavours, cf. sec. 3.1. Subleading coefficients are also beginning to emerge but at present not statistically significant yet. It has been noted that the convergence should speed up when constructing Padé approximants for the series, which also tends to increase the curvature towards larger μ [106,118]. Finally one should note that the continuum conversions relying on the two-loop beta function are certainly not reliable for these coarse lattices, while fits to non-perturbative beta functions tend to also increase the curvature.

5.6 The QCD phase diagram for $\mu \neq 0$ and the critical point

As in the case of $\mu = 0$, a determination of the order of the transition, and hence the search for the critical endpoint, is much harder, and we begin by discussing the qualitative picture. If a chemical potential is switched on for the light quarks, there is an additional parameter requiring an additional axis for our phase diagram characterizing the order of the transition, fig. 9 (right). This is shown in fig. 14, where the horizontal plane is spanned by the $\mu = 0$ phase diagram in $m_s, m_{u,d}$ and the vertical axis represents μ . The critical line separating the first order section from the crossover will now extend to finite μ and span a surface. A priori it

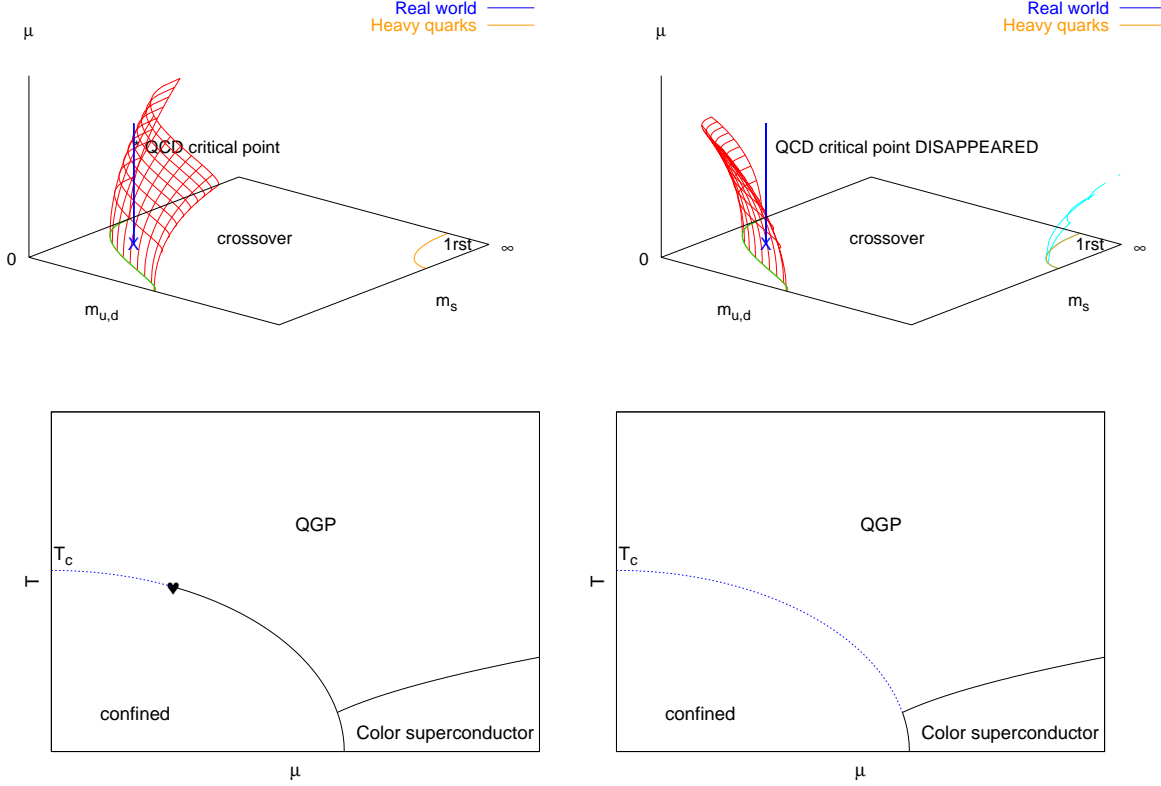


Fig. 14. Upper panel: The chiral critical surface in the case of positive (left) and negative (right) curvature. If the physical point is in the crossover region for $\mu = 0$, a finite μ phase transition will only arise in the scenario (left) with positive curvature, where the first-order region expands with μ . Note that for heavy quarks, the first-order region shrinks with μ , cf. sec. 5.9. Lower panel: phase diagrams for fixed quark mass (here $N_f = 3$) corresponding to the two scenarios depicted above.

is, of course, not known whether this surface might be leaning to the right or the left, or even have a more complicated behaviour as a function of the quark masses. However, the expected QCD phase diagram is only obtained if the left situation of fig. 14 is realized (unless there are additional critical surfaces yet unknown). The first order region expands as μ is turned on, so that the physical point, initially in the crossover region, eventually belongs to the critical surface. At that chemical potential μ_E , the transition is second order: that is the QCD critical point. Increasing μ further makes the transition first order. A completely different scenario arises if instead the first-order region shrinks as μ is turned on. In that case the physical point remains in the crossover region for any μ , fig. 14 (right).

There are then different strategies to determine the QCD phase diagram. One can fix a particular set of quark masses and for that theory switch on and increase the chemical potential to see whether a critical surface is crossed or not. Such calculations are covered in sec. 5.7. Alternatively, sec. 5.8 discusses how to start from the known critical line at $\mu = 0$ and study its evolution with a finite μ . That will give information on the whole phase diagram in fig. 14, including, eventually, physical QCD.

5.7 Critical point for fixed masses from reweighting and Taylor expansion

Reweighting methods produced the first finite density phase diagram from the lattice, obtained for light quarks corresponding to $m_\pi \sim 300$ MeV [119]. A later simulation at physical quark masses puts the critical point at $\mu_B^E \sim 360$ MeV [85], fig. 15 (left). In this work $L^3 \times 4$ lattices with $L = 6 - 12$ were used, working with the standard staggered fermion action.

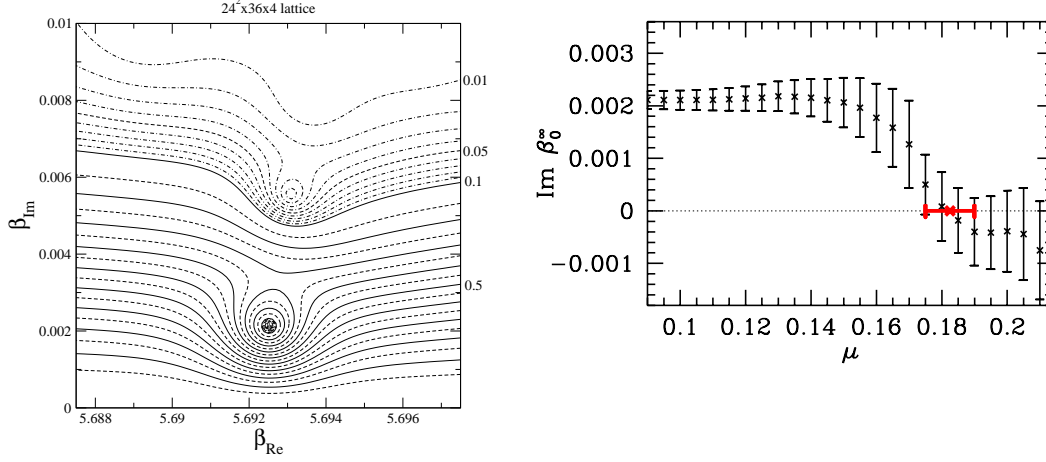


Fig. 15. Left: Lee-Yang zeroes in the complex β -plane for SU(3) pure gauge theory [120]. Right: Imaginary part of the Lee-Yang zero closest to the real axis as a function of chemical potential [85].

Quark masses were tuned to $m_{u,d}/T_c \approx 0.037$, $m_s/T_c \approx 1$, corresponding to the mass ratios $m_\pi/m_\rho \approx 0.19$, $m_\pi/m_K \approx 0.27$, which are close to their physical values. A Lee-Yang zero analysis [70] was employed in order to find the change from crossover behaviour at $\mu = 0$ to a first order transition for $\mu > \mu_E$. This is shown in fig. 15. For a crossover the partition function has zeroes only off the real axis, whereas for a phase transition the zero moves to the real axis when extrapolated to infinite volume. For a critical discussion of the use of Lee-Yang zeros in combination with reweighting, see [120]. Recently, reweighting has been combined with the density of states method [121], in order to extend the applicability of reweighting to larger values of μ/T . First interesting results have been obtained for $N_f = 4$, indicating a new high density phase and a possible triple point, where the high density transition line meets the deconfinement line [121]. Unfortunately, the method is computationally very expensive and so far limited to coarse and small lattices, so that it is difficult to unambiguously establish those findings at present.

In principle the determination of a critical point is also possible via the Taylor expansion. In this case true phase transitions will be signalled by an emerging non-analyticity, or a finite radius of convergence for the pressure series about $\mu = 0$ as the volume is increased. The radius of convergence of a power series gives the distance between the expansion point and the nearest singularity, and may be extracted from the high order behaviour of the series. A possible definition is

$$\rho = \lim_{n \rightarrow \infty} \rho_n \quad \text{with} \quad \rho_n = \left| \frac{c_0}{c_{2n}} \right|^{1/2n}. \quad (40)$$

General theorems ensure that if the limit exists and asymptotically all coefficients of the series are positive, then there is a singularity on the real axis. More details as well as previous applications to strong coupling expansions in various spin models can be found in [122]. In the series for the pressure such a singularity would correspond to the critical point in the (μ, T) -plane.

A critical endpoint for the $N_f = 2$ theory, based on this approach, was reported in [102]. The authors performed simulations on $L^3 \times 4$ lattices with $L = 8 - 24$, using the standard staggered action. The quark mass was fixed in physical units to $m/T_c = 0.1$. The aim of the simulations was to bracket the critical point by computing the Taylor coefficients of the quark number susceptibility up to sixth order (*i.e.* 8th order for the pressure) for various temperatures in the range $T/T_c = 0.75 - 2.15$, and extrapolate to finite μ . This was done for different lattice volumes in order to get an estimate of finite volume effects.

The results for the convergence radius eq. (40) are shown in fig. 16 (left). A rather strong volume dependence is apparent. While for the smaller 8^3 lattice the estimator ρ_n does not seem to converge to a finite radius of convergence, the results on the larger 24^3 lattice are

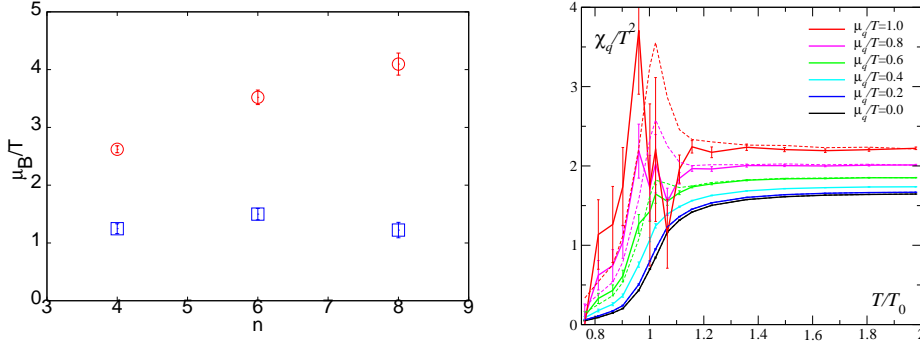


Fig. 16. Left: Estimators of the radius of convergence ρ_n , eq. (40), at $T/T_c = 0.95$ on $N_t = 4$ lattices. Circles represent $L = 8$, squares $L = 24$ [102]. Right: Quark number susceptibility computed through $O(\mu^4)$ (dashed lines) and $O(\mu^6)$ (solid lines) [101].

consistent with settling at a limiting value. Taking the large volume result at face value and extrapolating to all orders the estimate for the location of the critical point is $\mu_B^E/T_E = 1.1 \pm 0.2$ at $T_E/T_c(\mu = 0) = 0.95$ [102].

Another investigation of the two-flavour theory, also using the Taylor expansion of the pressure, is reported in [100,101]. This group works with a $16^3 \times 4$ lattice with p4-improved staggered fermions and a Symanzik-improved Wilson action, the quark mass is set to $m/T \approx 0.4$. The calculation to order μ^4 was performed in [100] while results on μ^6 are presented in [101]. The last work also contains detailed discussions of analytic calculations to compare with, namely the pressure in high temperature perturbation theory [123], which is going to hold at very high temperatures, as well as the hadron resonance gas model, which gives a rather good description of the pressure in the confined phase [124].

In agreement with [102] and qualitative expectations, their detailed results for the coefficients in the pressure series satisfy $c_6 \ll c_4 \ll c_2$ for $T > T_c$, *i.e.* one would have coefficients of order one for an expansion in $(\mu/\pi T)$. An impression of the convergence of the series can be obtained by looking at the quark number susceptibility calculated to consecutive orders, as shown in fig. 16 (right). For $T \lesssim 1.2T_c$, the series seems to converge rapidly and the μ^6 -result is compatible with the one through order μ^4 . Around the transition temperature T_c , the μ^4 -results show a peak emerging with growing μ/T_c , which in [100] was interpreted as evidence for a critical point. However, the μ^6 contribution suggests that in this region results do not yet converge, and the structure is hence not a significant feature of the full pressure. Furthermore, estimates for the radius of convergence through that order agreed with predictions from the hadron gas model, which however has infinite radius of convergence. Hence the conclusion in [101] that there is no signal for a critical point at that quark mass.

5.8 The change of the critical line with μ

Rather than fixing one set of masses and considering the effects of μ , one may map out the critical surface in fig. 14 by measuring how the $\mu = 0$ critical boundary line changes under the influence of μ . This question was addressed using an imaginary chemical potential in [81,82]. The methodology employed is the same as in sec. 4.4, *i.e.* measurement of the Binder cumulant of the chiral condensate. The results for $N_f = 3$ are summarized in fig. 17 (left). The chemical potential is found to have almost no influence on B_4 as a function of quark mass. A lowest-order fit, linear in am and $(a\mu)^2$, gives the error band fig. 17 (right), corresponding to

$$am^c(a\mu) = 0.0270(5) - 0.0024(160)(a\mu)^2. \quad (41)$$

Care must be taken for the conversion to physical units. The crucial point is that the gauge coupling β is tuned with changing μ to stay on the critical line, so that $a(\beta)$ decreases. Expressing the change of the critical quark mass with chemical potential in lattice and continuum

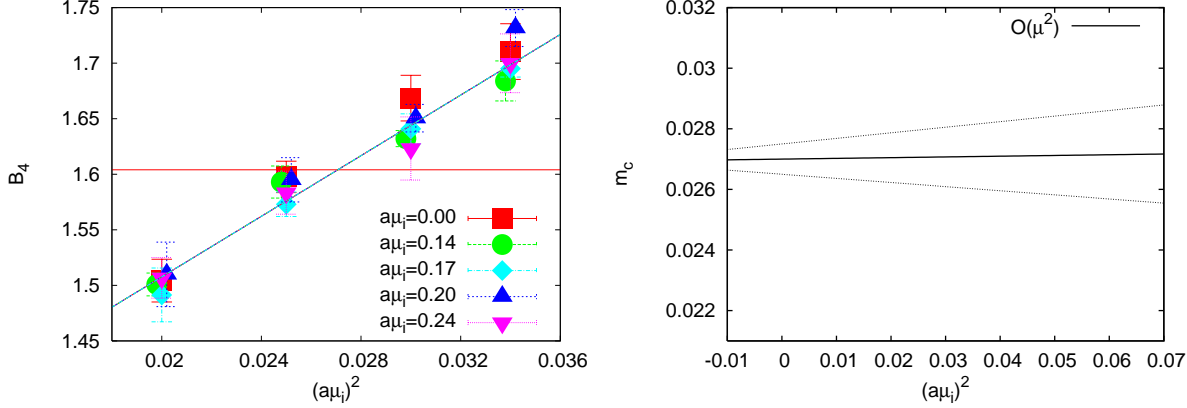


Fig. 17. Left: $B_4(am, a\mu_i)$ for $N_f = 3$, $N_t = 4$ and imaginary chemical potentials. Right: One-sigma error band for the critical mass $am^c(a\mu_i)$ resulting from a linear fit to the data on the left. From [82].

units as

$$\frac{am^c(\mu)}{am^c(0)} = 1 + \frac{c'_1}{am^c(0)}(a\mu)^2 + \dots, \quad \frac{m^c(\mu)}{m^c(0)} = 1 + c_1 \left(\frac{\mu}{\pi T} \right)^2 + \dots \quad (42)$$

then c_1 and c'_1 are related by

$$c_1 = \frac{\pi^2}{N_t^2} \frac{c'_1}{am^c(0)} + \left(\frac{1}{T_c(m, \mu)} \frac{dT_c(m^c(\mu), \mu)}{d(\mu/\pi T)^2} \right)_{\mu=0}. \quad (43)$$

Since c'_1 is observed to be nearly zero, it is the second term that dominates, leading to an overall negative coefficient $c_1 = -0.7(4)$ [82].

This is evidence that, in the $N_f = 3$ theory on an $N_t = 4$ lattice, the region of first-order transitions *shrinks* as a baryon chemical potential is turned on, and the “exotic scenario” of fig. 14 (right) is realized. Interestingly, similar qualitative conclusions are obtained from simulations of the three flavour theory with an isospin chemical potential [125], as well as simulations at imaginary μ employing Wilson fermions [109].

This investigation has also been extended to the case of non-degenerate quarks [82]. Fig. 18 (left) shows a comparison of the critical line for $\mu = 0$ with some critical masses calculated for a sizeable baryon chemical potential. The data show the same trend as for $N_f = 3$: the critical mass is nearly unchanged or slightly increasing with μ_i , in lattice units. The conversion to physical units proceeds as in the three flavour case and gives a dominant negative contribution to c_1 . Together with a very small value for c'_1 , it implies again that the first-order region shrinks as the baryon chemical potential is turned on, and the “exotic scenario” of fig. 14 (right) is the correct one.

5.9 The heavy quark limit: Potts model

In light of these surprising results, it is also interesting to consider the heavy quark corner of the schematic phase diagram of fig. 14. Simulations of quenched QCD at finite baryon number have been done in [126]. As the quark mass goes to infinity, quarks can be integrated out and QCD reduces to a gauge theory of Polyakov lines. First simulations of this theory with Wilson valence quarks can be found in [127]. At a second order phase transition, universality allows us to neglect the details of gauge degrees of freedom, so the theory reduces to the 3d three-state Potts model, which is in the 3d Ising universality class. Hence, studying the three-state Potts model should teach us about the behaviour of QCD in the neighbourhood of the critical line separating the quenched first order region from the crossover region. For large μ the sign problem in this theory has actually been solved by means of cluster algorithms [128].

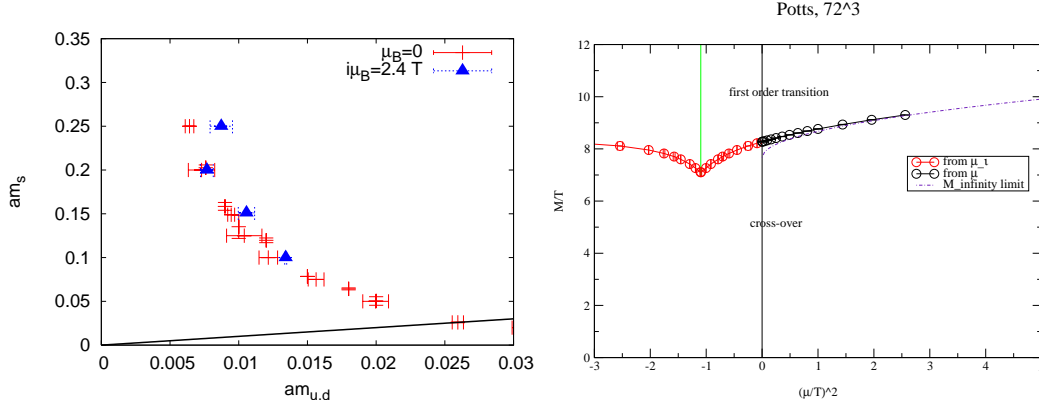


Fig. 18. Left: Comparison of the critical line at $\mu = 0$ and $a\mu_I = 0.2$. Right: The critical heavy quark mass separating first order from crossover as a function of μ^2 from the Potts model [129].

Here we are interested in simulations at small μ/T [129]. In this case, the sign problem is mild enough for brute force simulations at real μ to be feasible. In [129], the change of the critical heavy quark mass is determined as a function of real as well as imaginary μ , as shown in fig. 18 (right). Note that $M^c(\mu)$ rises with real chemical potential. *i.e.* the first order region in fig. 14 shrinks as finite baryon density is switched on. This system is thus an example of the non-standard scenario discussed in the previous section. The calculation also gives some insight in the problem of analytic continuation: while fig. 18 clearly endorses the approach in principle, an $O(\mu^8)$ -fit was required to reproduce the data on both sides of $\mu^2 = 0$. Similar accuracy is much more difficult to achieve around the chiral line with present resources.

5.10 Discussion of critical end point results

The results about the critical surface from sec. 5.8 appear to be in qualitative contradiction with those of [85], [102], which both conclude for the existence of a critical point (μ_E, T_E) at small chemical potential $\mu_E/T_E \lesssim 1$. However, in considering the reasons for such disagreement, one can see that the different data sets are actually not inconsistent with each other, and the differing pictures can be explained by standard systematic effects.

In [102] the critical point was inferred from an estimate of the radius of convergence of the Taylor expansion of the free energy. Regardless of the systematics when only 4 Taylor coefficients are available, the estimate is made for $N_f = 2$. The (μ, T) phase diagram of this theory might well be qualitatively different from that of $N_f = 2 + 1$ QCD, as illustrated in fig. 19 (right). Its critical endpoint point, obtained by intersecting a critical surface when going up vertically from the $N_f = 2$ quark mass values, is clearly a long way from the critical endpoint of physical QCD, and nothing follows quantitatively from the value of one for the other.

In [85] the double reweighting approach was followed. By construction, this reweighting is performed at a quark mass fixed in lattice units: $am_{u,d} = \frac{m_{u,d}}{T_c} = \text{const.}$ Since the critical temperature T_c decreases with μ , so does the quark mass. This decrease of the quark mass pushes the transition towards first order, which might be the reason why a critical point is found at small μ . This effect is illustrated in the sketch fig. 19 (left), where the bent trajectory intersects the critical surface, while the vertical line of constant physics does not. Put another way, [85] measures the analogue of c'_1 instead of c_1 in eq. (42). From fig. 15 (right) we see that the distance of the physical theory from criticality stays initially constant, consistent with a coefficient $c'_1 \approx 0$ as that in [82], sec. 5.8. Taking the variation $a(\mu)$ into account could then make a dominant contribution, which might possibly change the results qualitatively.

Conversely, in [82] only the leading order coefficient of $m^c(\mu)$ has been determined from imaginary μ . It cannot yet be excluded that there are cancelling terms of higher order, alter-

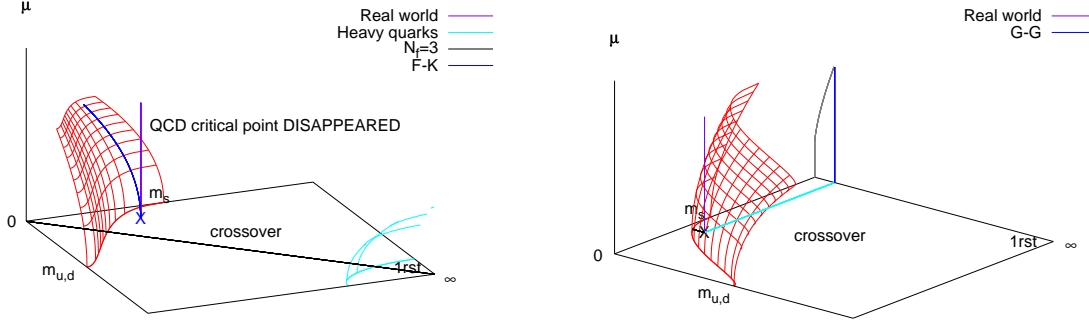


Fig. 19. Left: Effect of keeping the quark mass fixed in lattice units while changing μ , as in [85]. Right: Location of critical points for the $N_f = 2 + 1$ and the $N_f = 2$ theory, as considered in [102]. Knowing the latter does not predict the former.

nating in sign. Such contributions would no longer cancel after continuation to real μ , leading to a different picture. Knowledge of the next term in the series will clarify this.

On the other hand, a robust finding is the high quark mass sensitivity of the critical point: irrespective of the sign, if $c_1 \sim O(1)$ in eq. (42), $m^c(\mu)$ is a slowly varying function of μ , just as the pressure, screening masses or T_c . Hence $\mu_E(m)$ is rapidly varying. A change of quark masses by a few percent will then imply a change of μ_E by $O(100\%)$. One should also remember that most investigations so far have used unimproved staggered quarks on coarse $N_t = 4$ lattices only. This might be worrisome given the exceedingly light quarks involved, cf. sec. 2.2 and [8,93]. Finally, a more complicated picture with additional critical surfaces in fig. 14 is yet another possibility. In light of these circumstances even the qualitative features of the QCD phase diagram cannot be regarded as settled until they are probed with better accuracy on finer lattices.

6 Conclusions

We have summarized our current understanding of finite temperature and density QCD from numerical studies on the lattice. While many results in the pure gauge theory are available in the continuum limit, simulations with dynamical fermions still suffer from systematic errors. These are mainly due to the finite lattice spacing, and quark masses which don't meet their physical values yet. For the critical temperature and the equation of state these problems are now being tackled and the first continuum extrapolations become available.

Existing results provide us with a detailed picture of how equilibrium plasma properties change through the deconfinement transition up to a few T_c . Combinations of perturbative calculations and numerical simulations have produced insight into the regime of very high temperatures as well as the dynamics and mixing of hard and soft momentum modes. Altogether this provides a quantitative understanding of the relevant length scales in the plasma, as well as tests of the applicability of thermal perturbation theory.

The naive picture of the deconfined phase as a weakly interacting parton gas is not supported. For temperatures relevant to heavy ion collisions, the plasma displays strong residual interactions through soft gluonic modes, which cannot be treated perturbatively, and which influence different quantities in different ways. This gives a consistent explanation to the various observed features: the equation of state, susceptibilities and fermionic correlators are dominated by hard modes and not far from their ideal gas values, but the corrections are significant. Gluonic correlators, on the other hand, are dominated by soft modes and entirely off their leading perturbative predictions. An ideal gas is established only at asymptotically high temperatures.

Significant progress was made over the last five years regarding dynamical quantities as well as finite density simulations. In both fields methods have been developed, that are currently

being scrutinized for their reliability. Calculations of spectral functions provide a picture of remnant binding forces in the plasma phase as well as first semi-quantitative results for the transport coefficients. Calculations at finite density are now possible for $\mu/T \lesssim 1$, with good agreement between all methods whenever equal parameter sets are compared. However, the way to a quantitative understanding of the QCD phase diagram is still long, mainly due to the high quark mass and cut-off sensitivity of the critical endpoint. Current developments, also regarding computing speed-up for different fermion discretizations and improvement programmes, give reason to believe that these questions can be significantly improved upon in the near future.

References

1. J. R. Ellis, J. Phys. Conf. Ser. **50** (2006) 8 [[astro-ph/0504501](#)]; M. Laine, PoS **LAT2006** (2006) 014 [[hep-lat/0612023](#)]; M. Hindmarsh and O. Philipsen, Phys. Rev. D **71** (2005) 087302 [[hep-ph/0501232](#)].
2. K. Rajagopal and F. Wilczek, 2000, [[hep-ph/0011333](#)].
3. C. Gale and J. Kapusta, *Finite Temperature Field Theory* (Cambridge University Press, Cambridge, 2006); M. Le Bellac, *Thermal Field Theory* (Cambridge University Press, Cambridge, 1996).
4. A. D. Linde, Phys. Lett. B **100** (1981) 37; D. J. Gross, R. D. Pisarski and L. G. Yaffe, Rev. Mod. Phys. **53** (1981) 43.
5. W. Buchmüller and O. Philipsen, Nucl. Phys. B **443** (1995) 47 [[hep-ph/9411334](#)] and Phys. Lett. B **397** (1997) 112 [[hep-ph/9612286](#)]; G. Alexanian and V. P. Nair, Phys. Lett. B **352** (1995) 435 [[hep-ph/9504256](#)]; R. Jackiw and S. Y. Pi, Phys. Lett. B **403** (1997) 297 [[hep-th/9703226](#)]; J. M. Cornwall, Phys. Rev. D **57** (1998) 3694 [[hep-th/9710128](#)].
6. P. Hasenfratz and F. Karsch, Phys. Lett. B **125** (1983) 308.
7. I. Montvay and G. Münster, *Quantum Fields on a Lattice* (Cambridge University Press, Cambridge, 1994); J. Smit, *Introduction to Quantum Fields on a Lattice* (Cambridge University Press, Cambridge, 2002); T. DeGrand and C. DeTar, *Lattice Methods for Quantum Chromodynamics* (World Scientific, Singapore, 2006).
8. S. R. Sharpe, PoS **LAT2006** (2006) 022 [[hep-lat/0610094](#)]; S. Dürr, PoS **LAT2005** (2006) 021 [[hep-lat/0509026](#)].
9. D. J. Antonio *et al.* [RBC Collaboration], Phys. Rev. D **75** (2007) 114501 [[hep-lat/0612005](#)].
10. F. Niedermayer, Nucl. Phys. Proc. Suppl. **73** (1999) 105 [[hep-lat/9810026](#)].
11. R. Gupta, 1998, [[hep-lat/9807028](#)]; M. Lüscher, 1998, [[hep-lat/9802029](#)].
12. R. Sommer, Nucl. Phys. B **411** (1994) 839 [[hep-lat/9310022](#)].
13. A. Gray *et al.*, Phys. Rev. D **72**, 094507 (2005) [[hep-lat/0507013](#)].
14. L. D. McLerran and B. Svetitsky, Phys. Rev. D **24** (1981) 450.
15. L. G. Yaffe and B. Svetitsky, Phys. Rev. D **26** (1982) 963.
16. R. D. Pisarski and F. Wilczek, Phys. Rev. D **29**, 338 (1984); S. Gavin, A. Gocksch and R. D. Pisarski, Phys. Rev. D **49**, 3079 (1994) [[hep-ph/9311350](#)].
17. P. H. Ginsparg, Nucl. Phys. B **170** (1980) 388; T. Appelquist and R. D. Pisarski, Phys. Rev. D **23** (1981) 2305.
18. K. Kajantie, M. Laine, K. Rummukainen and M. E. Shaposhnikov, Nucl. Phys. B **503** (1997) 357 [[hep-ph/9704416](#)].
19. K. Kajantie, M. Laine, K. Rummukainen and M. E. Shaposhnikov, Nucl. Phys. B **458** (1996) 90 [[hep-ph/9508379](#)].
20. M. Laine, JHEP **9906** (1999) 020 [[hep-ph/9903513](#)].
21. A. Hart, M. Laine and O. Philipsen, Nucl. Phys. B **586** (2000) 443 [[hep-ph/0004060](#)].
22. M. Laine and Y. Schroder, JHEP **0503** (2005) 067 [[hep-ph/0503061](#)]; A. Hart and O. Philipsen, Nucl. Phys. B **572** (2000) 243 [[hep-lat/9908041](#)]; F. Karsch, E. Laermann and M. Lutgemeier, Phys. Lett. B **346** (1995) 94 [[hep-lat/9411020](#)]; L. Karkkainen *et al.*, Nucl. Phys. B **418** (1994) 3 [[hep-lat/9310014](#)]; G. S. Bali *et al.*, Phys. Rev. Lett. **71** (1993) 3059 [[hep-lat/9306024](#)].
23. F. Karsch, Lect. Notes Phys. **583** (2002) 209 [[hep-lat/0106019](#)].
24. G. Boyd *et al.*, Nucl. Phys. B **469** (1996) 419 [[hep-lat/9602007](#)].
25. Y. Iwasaki, K. Kanaya, T. Kaneko and T. Yoshie, Phys. Rev. D **56** (1997) 151 [[hep-lat/9610023](#)].
26. E. Laermann and O. Philipsen, Ann. Rev. Nucl. Part. Sci. **53** (2003) 163 [[hep-ph/0303042](#)].
27. A. Ali Khan *et al.* [CP-PACS Collaboration], Phys. Rev. D **63** (2001) 034502 [[hep-lat/0008011](#)].
28. F. Karsch, E. Laermann and A. Peikert, Nucl. Phys. B **605** (2001) 579 [[hep-lat/0012023](#)].
29. M. Cheng *et al.*, Phys. Rev. D **74** (2006) 054507 [[hep-lat/0608013](#)].
30. Y. Aoki, Z. Fodor, S. D. Katz and K. K. Szabo, Phys. Lett. B **643** (2006) 46 [[hep-lat/0609068](#)].
31. J. Engels *et al.*, Phys. Lett. B **252** (1990) 625.
32. F. Karsch, E. Laermann and A. Peikert, Phys. Lett. B **478** (2000) 447 [[hep-lat/0002003](#)].
33. Y. Aoki, Z. Fodor, S. D. Katz and K. K. Szabo, JHEP **0601** (2006) 089 [[hep-lat/0510084](#)].
34. C. Bernard *et al.*, Phys. Rev. D **75** (2007) 094505 [[hep-lat/0611031](#)].
35. K. Kajantie, M. Laine, K. Rummukainen and Y. Schroder, Phys. Rev. D **67** (2003) 105008 [[hep-ph/0211321](#)].
36. A. Hietanen *et al.*, JHEP **0501** (2005) 013 [[hep-lat/0412008](#)].
37. F. Di Renzo *et al.*, JHEP **0607** (2006) 026 [[hep-ph/0605042](#)].

38. B. Grossmann, S. Gupta, U. M. Heller and F. Karsch, Nucl. Phys. B **417** (1994) 289 [hep-lat/9309007].
39. S. Datta and S. Gupta, Nucl. Phys. B **534** (1998) 392 [hep-lat/9806034].
40. S. Gupta, Phys. Rev. D **60** (1999) 094505 [hep-lat/9903019].
41. S. Datta and S. Gupta, Phys. Rev. D **67** (2003) 054503 [hep-lat/0208001].
42. E. Laermann and P. Schmidt, Eur. Phys. J. C **20** (2001) 541 [hep-lat/0103037].
43. P. de Forcrand *et al.* [QCD-TARO Collaboration], Phys. Rev. D **63** (2001) 054501 [hep-lat/0008005].
44. R. V. Gavai and S. Gupta, Phys. Rev. D **67** (2003) 034501 [hep-lat/0211015].
45. R. V. Gavai, S. Gupta and P. Majumdar, Phys. Rev. D **65** (2002) 054506 [hep-lat/0110032].
46. M. Laine, private communication.
47. T. Matsui and H. Satz, Phys. Lett. B **178** (1986) 416.
48. A. Mocsy and P. Petreczky, [arXiv:0705.2559 [hep-ph]].
49. O. Kaczmarek, F. Karsch, E. Laermann and M. Lutgemeier, Phys. Rev. D **62** (2000) 034021 [hep-lat/9908010].
50. R. D. Pisarski and O. Alvarez, Phys. Rev. D **26** (1982) 3735.
51. S. Nadkarni, Phys. Rev. D **33** (1986) 3738.
52. U. M. Heller, F. Karsch and J. Rank, Phys. Rev. D **57** (1998) 1438 [hep-lat/9710033].
53. F. Karsch, E. Laermann and A. Peikert, Nucl. Phys. B **605** (2001) 579 [hep-lat/0012023].
54. C. DeTar, O. Kaczmarek, F. Karsch and E. Laermann, Phys. Rev. D **59** (1999) 031501 [hep-lat/9808028].
55. V. Bornyakov *et al.*, Nucl. Phys. Proc. Suppl. **119** (2003) 703 [hep-lat/0209157].
56. S. Nadkarni, Phys. Rev. D **34** (1986) 3904.
57. O. Philipsen, Phys. Lett. B **535** (2002) 138 [hep-lat/0203018].
58. O. Jahn and O. Philipsen, Phys. Rev. D **70** (2004) 074504 [hep-lat/0407042].
59. M. Asakawa, T. Hatsuda and Y. Nakahara, Prog. Part. Nucl. Phys. **46** (2001) 459 [hep-lat/0011040].
60. G. Aarts and J. M. Martinez Resco, JHEP **0204** (2002) 053 [hep-ph/0203177].
61. T. Umeda, K. Nomura and H. Matsufuru, Eur. Phys. J. C **39S1** (2005) 9 [hep-lat/0211003]; M. Asakawa and T. Hatsuda, Phys. Rev. Lett. **92** (2004) 012001 [hep-lat/0308034]; S. Datta, F. Karsch, P. Petreczky and I. Wetzorke, Phys. Rev. D **69** (2004) 094507 [hep-lat/0312037]; A. Jakovac, P. Petreczky, K. Petrov and A. Velytsky, Phys. Rev. D **75** (2007) 014506 [hep-lat/0611017].
62. G. Aarts *et al.*, [arXiv:0705.2198 [hep-lat]].
63. R. Morrin *et al.*, PoS **LAT2005** (2006) 176 [hep-lat/0509115].
64. A. Nakamura and S. Sakai, Phys. Rev. Lett. **94** (2005) 072305 [hep-lat/0406009].
65. H. B. Meyer, 2007, [arXiv:0704.1801 [hep-lat]].
66. G. Aarts *et al.*, Phys. Rev. Lett. **99** (2007) 022002 [arXiv:hep-lat/0703008].
67. M. Laine, O. Philipsen, P. Romatschke and M. Tassler, JHEP **0703** (2007) 054 [hep-ph/0611300].
68. M. Laine, JHEP **0705** (2007) 028 [arXiv:0704.1720 [hep-ph]].
69. M. Laine, O. Philipsen and M. Tassler, [arXiv:0707.2458 [hep-lat]].
70. C. N. Yang and T. D. Lee, Phys. Rev. **87** (1952) 404; Phys. Rev. **87** (1952) 410.
71. M. A. Halasz *et al.*, Phys. Rev. D **58** (1998) 096007 [hep-ph/9804290].
72. F. Karsch, Phys. Rev. D **49**, 3791 (1994) [hep-lat/9309022].
73. A. Ali Khan *et al.* [CP-PACS Collaboration], Phys. Rev. D **63**, 034502 (2001) [hep-lat/0008011]; Y. Iwasaki, K. Kanaya, S. Kaya and T. Yoshie, Phys. Rev. Lett. **78**, 179 (1997) [hep-lat/9609022].
74. C. W. Bernard *et al.* [MILC Collaboration], Phys. Rev. D **61**, 111502 (2000) [hep-lat/9912018]; E. Laermann, Nucl. Phys. Proc. Suppl. **60A**, 180 (1998).
75. S. Chandrasekharan and C. G. Strouthos, Phys. Rev. D **69**, 091502 (2004) [hep-lat/0401002]; S. Chandrasekharan and F. J. Jiang, Phys. Rev. D **68**, 091501 (2003) [hep-lat/0309025].
76. M. D'Elia, A. Di Giacomo and C. Pica, Phys. Rev. D **72** (2005) 114510 [hep-lat/0503030]; G. Cossu, M. D'Elia, A. Di Giacomo and C. Pica, [arXiv:0706.4470 [hep-lat]].
77. J. B. Kogut and D. K. Sinclair, Phys. Rev. D **73** (2006) 074512 [hep-lat/0603021].
78. S. Chandrasekharan and A. C. Mehta, [arXiv:0705.0617 [hep-lat]].
79. F. Karsch, E. Laermann and C. Schmidt, Phys. Lett. B **520**, 41 (2001) [hep-lat/0107020].
80. N. H. Christ and X. Liao, Nucl. Phys. Proc. Suppl. **119**, 514 (2003).
81. P. de Forcrand and O. Philipsen, Nucl. Phys. B **673**, 170 (2003) [hep-lat/0307020].
82. P. de Forcrand and O. Philipsen, JHEP **0701** (2007) 077 [hep-lat/0607017].

83. H. W. Blote, E. Luijten and J.R. Heringa, J. Phys. A: Math. Gen. **28** (1995) 6289.
84. P. Braun-Munzinger, K. Redlich and J. Stachel, 2003, [[nucl-th/0304013](#)].
85. Z. Fodor and S. D. Katz, JHEP **0404**, 050 (2004) [[hep-lat/0402006](#)].
86. Z. Szep, PoS **JHW2005** (2006) 017 [[hep-ph/0512241](#)].
87. Y. Aoki *et al.*, Nature **443** (2006) 675 [[hep-lat/0611014](#)].
88. O. Philipsen, PoS **LAT2005** (2006) 016 [[hep-lat/0510077](#)].
89. C. Schmidt, PoS **LAT2006** (2006) 021 [[hep-lat/0610116](#)].
90. I. M. Barbour *et al.*, Nucl. Phys. Proc. Suppl. **60A**, 220 (1998) [[hep-lat/9705042](#)].
91. Z. Fodor and S. D. Katz, Phys. Lett. B **534**, 87 (2002) [[hep-lat/0104001](#)].
92. F. Csikor *et al.*, JHEP **0405**, 046 (2004) [[hep-lat/0401016](#)].
93. M. Golterman, Y. Shamir and B. Svetitsky, Phys. Rev. D **74** (2006) 071501 [[hep-lat/0602026](#)].
94. S. A. Gottlieb *et al.*, Phys. Rev. Lett. **59** (1987) 2247.
95. P. de Forcrand *et al.* [QCD-TARO Collaboration], Nucl. Phys. Proc. Suppl. **73**, 477 (1999) [[hep-lat/9810057](#)].
96. A. Hart, M. Laine and O. Philipsen, Phys. Lett. B **505**, 141 (2001) [[hep-lat/0010008](#)].
97. R. V. Gavai and S. Gupta, Phys. Rev. D **68**, 034506 (2003) [[hep-lat/0303013](#)].
98. C. R. Allton *et al.*, Phys. Rev. D **66**, 074507 (2002) [[hep-lat/0204010](#)].
99. F. Karsch *et al.*, Nucl. Phys. Proc. Suppl. **129** (2004) 614 [[hep-lat/0309116](#)].
100. C. R. Allton *et al.*, Phys. Rev. D **68**, 014507 (2003) [[hep-lat/0305007](#)].
101. C. R. Allton *et al.*, Phys. Rev. D **71**, 054508 (2005) [[hep-lat/0501030](#)].
102. R. V. Gavai and S. Gupta, Phys. Rev. D **71**, 114014 (2005) [[hep-lat/0412035](#)].
103. M. P. Lombardo, Nucl. Phys. Proc. Suppl. **83**, 375 (2000) [[hep-lat/9908006](#)].
104. P. de Forcrand and O. Philipsen, Nucl. Phys. B **642**, 290 (2002) [[hep-lat/0205016](#)].
105. M. D'Elia and M. P. Lombardo, Phys. Rev. D **67**, 014505 (2003) [[hep-lat/0209146](#)].
106. M. D'Elia and M. P. Lombardo, Phys. Rev. D **70**, 074509 (2004) [[hep-lat/0406012](#)].
107. V. Azcoiti, G. Di Carlo, A. Galante and V. Laliena, JHEP **0412**, 010 (2004) [[hep-lat/0409157](#)] and Nucl. Phys. B **723**, 77 (2005) [[hep-lat/0503010](#)].
108. H. S. Chen and X. Q. Luo, Phys. Rev. D **72**, 034504 (2005) [[hep-lat/0411023](#)].
109. H. S. Chen and X. Q. Luo, 2007, [hep-lat/0702025](#).
110. A. Roberge and N. Weiss, Nucl. Phys. B **275**, 734 (1986).
111. M. G. Alford, A. Kapustin and F. Wilczek, Phys. Rev. D **59** (1999) 054502 [[hep-lat/9807039](#)].
112. P. de Forcrand and S. Kratochvila, PoS **LAT2005** (2006) 167 [[hep-lat/0509143](#)] and Nucl. Phys. Proc. Suppl. **153** (2006) 62 [[hep-lat/0602024](#)].
113. A. Alexandru, M. Faber, I. Horvath and K. F. Liu, Phys. Rev. D **72** (2005) 114513 [[hep-lat/0507020](#)].
114. F. Csikor *et al.*, JHEP **0405** (2004) 046 [[hep-lat/0401016](#)].
115. Z. Fodor, S. D. Katz, K. K. Szabo and A. I. Toth, Nucl. Phys. Proc. Suppl. **140** (2005) 508 [[hep-lat/0410032](#)].
116. S. Hands, Nucl. Phys. Proc. Suppl. **106** (2002) 142 [[hep-lat/0109034](#)]; S. Chandrasekharan, Nucl. Phys. Proc. Suppl. **94** (2001) 71 [[hep-lat/0011022](#)]; O. Philipsen, Nucl. Phys. Proc. Suppl. **94** (2001) 49 [[hep-lat/0011019](#)].
117. N. Kawamoto, K. Miura, A. Ohnishi and T. Ohnuma, Phys. Rev. D **75** (2007) 014502 [[hep-lat/0512023](#)].
118. M. P. Lombardo, PoS **LAT2005** (2006) 168 [[hep-lat/0509181](#)].
119. Z. Fodor and S. D. Katz, JHEP **0203**, 014 (2002) [[hep-lat/0106002](#)].
120. S. Ejiri, 2005, [[hep-lat/0506023](#)].
121. Z. Fodor, S. D. Katz and C. Schmidt, JHEP **0703** (2007) 121 [[hep-lat/0701022](#)].
122. J. M. Drouffe and J. B. Zuber, Phys. Rept. **102**, 1 (1983).
123. A. Vuorinen, Phys. Rev. D **68**, 054017 (2003) [[hep-ph/0305183](#)].
124. F. Karsch, K. Redlich and A. Tawfik, Eur. Phys. J. C **29**, 549 (2003) [[hep-ph/0303108](#)].
125. D. K. Sinclair and J. B. Kogut, 2006, [[hep-lat/0609041](#)].
126. J. Engels, O. Kaczmarek, F. Karsch and E. Laermann, Nucl. Phys. B **558**, 307 (1999) [[hep-lat/9903030](#)].
127. R. De Pietri, A. Feo, E. Seiler and I. O. Stamatescu, 2007, [[arXiv:0705.3420](#) [[hep-lat](#)]].
128. M. G. Alford, S. Chandrasekharan, J. Cox and U. J. Wiese, Nucl. Phys. B **602**, 61 (2001) [[hep-lat/0101012](#)].
129. S. Kim, Ph. de Forcrand, S. Kratochvila and T. Takaishi, PoS **LAT2005** (2006) 166 [[hep-lat/0510069](#)].